Science Advances
AAAS

Supplementary Materials for

Cell patterning by secretion-induced plasma membrane flows

Veneta Gerganova, Iker Lamas, David M. Rutkowski, Aleksandar Vještica, Daniela Gallo Castro, Vincent Vincenzetti, Dimitrios Vavylonis*, Sophie G. Martin*

*Corresponding author. Email: sophie.martin@unil.ch (S.G.M.); vavylonis@lehigh.edu (D.V.)

Published 17 September 2021, *Sci. Adv.* **7**, eabg6718 (2021)
DOI: 10.1126/sciadv.abg6718

The PDF file includes:

Other Supplementary Material for this manuscript includes the following:

SUPPLEMENTARY METHODS

Determination of membrane diffusion and dissociation rates by FRAP

Diffusion coefficients and membrane dissociation constants were determined by fitting FRAP recovery profiles to a 1D model (Fig S4). The method relies on the different effects of diffusion and association/dissociation on the recovery, with diffusion providing smoothing of profile over time (*71*) and association/dissociation contributing to uniform recovery.

Experimental FRAP profiles. Experimental fluorescence intensity profiles were acquired after photobleaching of a rectangular region and imaging, on the top surface of *S. pombe* cells (Fig S4A; see experimental details in the experimental methods). We corrected for photobleaching after the initial FRAP event by multiplying all intensities by e^{kt} after background subtraction, where k is the exponential decay constant of the average intensity of a neighboring non-bleached cell. From these photobleach-corrected images we determined the intensity profile $I(x,t)$ by defining a rectangular region of interest along the long axis of a bleached cell with width ~2 μm, excluding the region close to the cell tips, and calculated the average intensity along this line at points spaced 0.0425 μm (1 pixel) apart through the bleaching recovery using ImageJ's getProfile function (Fig S4B).

Model with diffusion and association/dissociation used for fitting. To match the experimental bleach recovery, we modelled the evolution of the concentration profile of a membrane-associated protein, $c_m(x,t)$, along a 1D line with reflecting boundaries at positions x_a, x_b, defining the size of the finite membrane reservoir (approximately the location of cell poles and beyond, to include the back side of the cell). The x-dimension in the model corresponds to the long axis of the cell. We assumed $c_m(x,t)$ obeys the following equations, which include both the effects of diffusion and membrane binding/unbinding:

$$\frac{\partial c_m(x,t)}{\partial t} = D\frac{\partial^2 c_m(x,t)}{\partial x^2} - k_{off}c_m(x,t) + k_{on}C(t)$$
$$C(t) = C_{tot} - \int_{x_a}^{x_b} c_m(x,t)dx\,, \qquad (5)$$

where c_m is concentration on the membrane , C is the number of proteins in the cytoplasm, C_{tot} is the total number of proteins, and k_{off} , k_{on} are the membrane dissociation and association rate constants. We do not write a separate diffusion equation for the cytoplasm, assuming that cytoplasmic diffusion is sufficiently fast. We also specifically consider the limit where most of the proteins are on the membrane: $C(t) \ll C_{tot}$, (equivalently, the limit of sufficiently large k_{on}). The Green's function describing the probability for a single protein being at position x at time t, given that it was at position x_0 at time $t = 0$ is

$$p(x,t|x_0,0) = \mathrm{e}^{-k_{off}t}p_D(x,t) + \frac{1-\mathrm{e}^{-k_{off}t}}{x_b-x_a}, \qquad (6)$$

where $p_D\,(x,t)$ accounts for the probability of the particle position due to diffusion alone:

$$p_D(x,t|x_0,0) = \frac{1}{x_b-x_a} + \frac{2}{x_b-x_a}\sum_{n=1}^{\infty} e^{-Dt\lambda_n^2}\cos\big(\lambda_n(x-x_a)\big)\cos\big(\lambda_n(x_0-x_a)\big)\text{ , where }\lambda_n = \frac{n\pi}{x_b-x_a} \qquad (7)$$

General procedure of fitting experimental I(x,t) profiles. Assuming $c_m(x,t)$ is proportional to the experimental $I(x,t)$, we solve for $c_m(x,t)$ given an initial condition $c_m(x,0)$ that is proportional to the intensity profile imaged immediately after the photobleaching, $I(x,0)$. We then fit the model

to both *x* and *t* after photobleaching simultaneously, using SciPy's optimization curve fitting to get a single best fit value for *D* and k_{off} as described below. The sum in Eq. (7) was carried up to n = 500. We checked that replacing this by 250 did not have a significant effect on the values determined for *D* and k_{off} for our experimental data.

Evaluation of initial intensity distribution and simulation boundary positions x_a and x_b. The intensity profile is divided into three regions: left, middle, and right (Fig S4B). The intensity in the middle region, defined to be between x_d and x_e where $x_a \leq x_d \leq x_e \leq x_b$, is determined by the intensity profile I_i^0 immediately after photobleaching, evaluated at pixels *i* of the projected profile, corresponding to positions x_i (Fig S4B). The middle region is therefore treated as a sum of $n = \Delta x/(x_e - x_d)$ separate integrals, where Δx is the pixel size. The lengths of the left and right flanking regions are both equal to l_F, with $l_F = x_d - x_a = x_b - x_e$. We average the intensity of the pre-bleached cell over the middle region and set this as the initial intensity of the two flanking regions, I_F^0. The value of l_F determines the uniform intensity at long times, I_∞, according to mass conservation:

$$(2l_F + x_e - x_d)I_\infty = \sum_{i=0}^{n} I_i^0 \Delta x + 2l_F I_F^0. \quad (8)$$

The long time intensity I_∞, or equivalently l_F, is determined via the fitting procedure. In mutants where the l_F value drifted towards 0 or large numbers, it was restricted to be in the range 2-10 μm.

Evolution of concentration on a discrete lattice starting from a given initial condition. The equation describing the concentration or intensity as a function of position x_i corresponding to pixel *i* , and time is found by integration, $I_{model}(x_i, t) = \int_{x_a}^{x_b} I(x', 0)p(x_i, t|x', 0)dx'$, which, using Equations (6) and (7) gives:

$$I_{model}(x_i, t) = \frac{1}{x_b - x_a}\left[2l_F I_F^0 + \frac{1}{2}\sum_{i=0}^{n}(I_i^0 + I_{i+1}^0)\Delta x\right] + \frac{2\exp(-k_{off}t)}{x_b - x_a}\left[I_F^0 S_{x_a,x_d}(x_i, t) + I_F^0 S_{x_e,x_b}(x_i, t) + \frac{1}{2}\sum_{j=0}^{n}(I_j^0 + I_{j+1}^0)S_{x_j,x_{j+1}}(x_i, t)\right] \quad (9)$$

where $S_{x_1,x_2}(x,t) = \sum_{m=1}^{\infty} \frac{e^{-Dt\lambda_m^2}}{\lambda_m}\cos(\lambda_m(x - x_a))\left[\sin(\lambda_m(x_2 - x_a)) - \sin(\lambda_m(x_1 - x_a))\right]$ and λ_n is given in Equation (7). Here, the initial intensity $I(x, 0)$ at $x_i < x < x_{i+1}$ was assumed to be given by $0.5(I_i^0 + I_{i+1}^0)$. An example of a fit over time to the experimental FRAP data for a cell expressing 1xRitC-GFP using this expression is shown in Fig S4C.

Accuracy of determining D and k_{off}. The fit to each FRAP profile determines the single best fit values for *D* and k_{off} for each cell, corresponding to the largest R^2 value that is a measure of the goodness of the fit. These two values are not independent of each other: since both contribute to recovery, increasing the value of one parameter can be partly compensated by a decrease in the other (even though they influence the evolution of the profile differently, depending on the size of the bleached region). Additionally, one of the two parameters may be too small and thus dominated by the other. These complications are reflected in a large scatter of values for *D* and k_{off} among cells (Fig 3A, 4B and 5G). To check that despite this scatter, averaging over cells is meaningful, we developed a global procedure to determine the best *D* and k_{off} simultaneously for all cells. For

each cell of a given cell type, we varied D and k_{off} over six orders of magnitude and calculated the R^2 value. We then plotted the R^2 value as function of D and k_{off}, averaged over all cells of the same cell type (Fig S4D-F). The best fitting regions indicated by high values of R^2 typically form a pair of branches: one horizontal (constant k_{off}) and the other vertical (constant D) which intersect to form a curved bend. The median of the best fit value for D and k_{off} as determined by the 1D model is indicated by a red circle. For most photobleached proteins this highest average R^2 (indicated by a blue circle) is close to the median of the best fit values from the 1D model. One case does not show particularly good consistency (1x cc-CBD-Δ2), where the highest average R^2 is at very low values of k_{off}), suggesting that the values determined for D and k_{off} for these proteins is not reliable. Vertical or horizontal regions of high R^2 that extend beyond the boundaries of the graphs also indicate that the parameter varied along such a region may only be determined up to an upper limit. They typically correspond to scattered D and k_{off} values in Fig 3A, 4B and 5G. Finally, the line defining the ridge of the pair of branches that intersect to form a curved bend in Fig S4D,E is plotted as continuous line in Fig 3A,D and 4D to indicate the different combinations of D and k_{off} that provide similar overall recovery.

Simulations to validate FRAP fitting procedure. One limitation of our FRAP fit method to extract D and k_{off} is that we neglect the diffusion along the radial cylindrical direction. To examine the implications of this limitation, as well as another check of our method, we simulated FRAP experiments accounting for diffusion and membrane association/dissociation of particles on the surface of a cylinder with reflecting boundary conditions at the ends. We used a similar method as used for the sphere model with 50,000 particles on the surface of a cylinder with radius 2 μm and length 12 μm. As with the discrete sphere model, we fix $k_{on} = 0.01\ s^{-1}$. The displacement is calculated as $\sqrt{2D\Delta t}\xi(t)$ independently in both directions in the plane tangent to the cylinder surface, where Δt is the timestep determined from the Gillespie algorithm and $\xi(t)$ is a random Gaussian distributed variable with zero mean and unit variance. The displacement along the long axis of the cylinder needs no modification, but the displacement in the radial direction is projected down onto the cylinder surface while maintaining the distance as with the sphere model. To ensure that the radial diffusion is properly implemented, we measure the change in the azimuthal angle, $\langle\phi(t)^2\rangle$, as a function of time up to a time step of 1000 s, similar to Fig S9A.

The bleaching recovery was measured over a region of width 2.36 μm which is similar to the average experimental width of experimental cells. We took snapshots of particle positions every 1 s for a total of 500 s. To simulate initial photobleaching we label particles on the surface which are within a certain region at a given frame number as being bleached. This simulated bleach region is rectangular on the surface of the cylinder with a long axis of 3.315 μm and an arc length of half the circumference. To calculate the simulated intensity profile, $I_{sim}(x,t)$, we counted the number of particles in this region over time that were not labelled as being bleached in the initial frame and further assume that the intensity is proportional to the number of particles. To get better averages for the bleaching recovery, we simulate box photobleaching at each snapshot and follow the k independent recovery trajectories from their respective bleached frame, where k is the number of snapshots. We then average the intensity curves for each bleaching recovery at the same amount of time passed since the bleaching frame to obtain $\langle I_{sim}(x,t)\rangle$. We then use $\langle I_{sim}(x,t)\rangle$ up to a time of 250 s as the input for the 1D model to predict D and k_{off}. When using $D = 10^{-3}$ μm^2/s and $k_{off} = 10^{-2}$ /s for input parameter values of the discrete simulations, which are approximately in the range of 2xRitC-GFP, there is good agreement between the values inputted

into the simulations i.e. the values determined by the R^2 plot (red circle), and the values determined by the 1D model (Fig S4D). This result indicates that the 1D model can correctly predict D and k_{off} values. For input parameters with zero diffusion ($D = 0$, $k_{off} = 10^{-2}$ /s) and zero membrane unbinding ($D = 10^{-3}$ μm^2/s, $k_{off} = 0$) shown in Fig S4G the red dashed line indicates the non-zero input parameters are accurately determined, however a small nonzero value is assigned to the other parameter.

Comments on measured D and k_{off} *values.* Even though the estimated values of *D* or k_{off} can be partly compensated by an inverse change in the other, the FRAP recovery fits to the 1xRitC, 2xRitC, 3xRitC constructs do indicate that the main parameter responsible for slowing dynamics with increasing number of RitC domains is k_{off} (Fig S4E). This trend most likely indicates the cooperative nature of the dissociation process for constructs with multiple binding sites (*77*). Our results also point to a reduction of the diffusion coefficient with increasing number *n* of RitC domains stronger than 1/*n*, unlike prior experiments in supported bilayers where the measured diffusion coefficient of membrane-associated proteins was inversely proportional to the number of bound lipids (*78*), and theoretical calculations based on the Saffman-Delbrück model predicting an even weaker scaling in the dilute limit (*78*). However more precise measurements are needed to resolve if such a reduction is consistent with the expected size dependence of *D* in dilute systems (*78, 79*) or else if this is an indication of crowding mechanisms and microdomain formation in the fluid membrane component (*80, 81*). Interestingly, our measurements also indicate slower diffusion of 3xsfGP-1xRitC compared to sfGP-1xRitC. This observation could indicate that cytoplasmic drag might dominate diffusion of the 3xsfGP construct; further studies could explore if this diffusion reflects size-dependent frictional interaction with cytoplasm adjacent to inner membrane leaflet or else if it is due to oligomerization and related processes.

Image analysis of concentration profiles

All image-processing analyses were performed with Image J software (http://rsb.info.nih.gov/ij/). Image and time-lapse recordings were imported to the software using the Bio-Formats plugin (http://loci.wisc.edu/software/bio-formats). Time-lapse recordings were aligned using the StackReg plugin (https://sites.imagej.net/BIG-EPFL/) using the rigid body method. All optogenetic data analyses were performed using MATLAB (R2019a), with scripts developed in-house. Figures were assembled with Adobe Photoshop CC2019 and Adobe Illustrator 2020.

Correlating CRY2PHR-mCherry tip depletion dynamics with endogenous GFP-tagged protein signal intensities at cell tips.

CRY2PHR-mCherry tip depletion dynamics was monitored in strains co-expressing CRIB (N = 3, n = 275 cells), Ypt3 (N = 3, n = 184 cells), Exo84 (N = 3, n = 290 cells) and Exo70 (N = 3, n = 281 cells) GFP-tagged proteins (sample strains) in normal conditions (Fig 1B and S1C-E); in strains co-expressing CRIB-3GFP and GFP-Ypt3 treated with BFA (CRIB: N = 3, n = 219 cells; Ypt3: N = 3, n = 230 cells) or ethanol as control (CRIB: N = 3, n = 127 cells; Ypt3: N = 3, n = 136 cells); in *ypt3-i5* CRIB-3GFP and *ypt3*+ CRIB-3GFP strains at 25 ° C (*ypt3*+ CRIB-3GFP: N = 3, n = 191 cells; *ypt3-i5* CRIB-3GFP: N = 3, n = 132 cells) and 36 °C (*ypt3*+ CRIB-3GFP: N = 3, n = 229 cells; *ypt3-i5* CRIB-3GFP: N = 3, n = 204 cells); and in *sty1*Δ CRIB-3GFP strain treated with LatA (N = 3, n = 276 cells) or left untreated (N = 3, n = 293

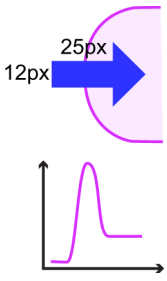

cells). Tip depletion was assessed upon photoactivation of the CRY2-CIB1 system by recording the RFP fluorescence intensity over an ROI that was 12 pixels wide by 25 pixels long (≈ 1 μm by 2.075 μm) and drawn perpendicular to the cell tip cortex over 20 timepoints, as shown by the blue arrow in the scheme on the right. The RFP and GFP fluoresce profiles across the plasma membrane were recorded over time. The GFP signal was used to correlate the presence of endogenous proteins with the CRY2PHR-mCherry tip depletion dynamics. Note that in these sets of experiments the initial timepoint was not included in the analysis, since CRY2PHR does not yet achieve its maximal plasma membrane recruitment (see Fig 3B). Thus, the second time point was set as the initial timepoint (t_0) in these experiments (19 timepoints in total). This corresponds to t = 0 s in Fig 3B.

To derive photobleaching correction coefficients, the average camera background signals (*Bckg*) from 6 cell-free regions were measured; and fluorophore bleaching was measured from entire cells, using RFP controls for RFP and sample cells for GFP.

$$\boldsymbol{RFP\ bleaching\ correction\ coefficient} = \left(RFP\ Intensity\ of\ cell_{tn} - Bckg_{tn}\right) \Big/ \left(RFP\ Intensity\ of\ cell_{t0} - Bckg_{t0}\right) \quad \text{(E1)}$$

$$\boldsymbol{GFP\ bleaching\ correction\ coefficient} = \left(GFP\ Intensity\ of\ cell_{tn} - Bckg_{tn}\right) \Big/ \left(GFP\ Intensity\ of\ cell_{t0} - Bckg_{t0}\right) \quad \text{(E2)}$$

where *RFP Intensity* and *GFP Intensity* of cell stands for the signal measured from entire RFP control and sample cells, respectively; *Bckg* stands for the average fluorescence intensity of 6 independent cell-free regions; t_n represents a given time point along the time course of the experiment; and t_0 represents the initial time point (n = 19 time points). These coefficients were corrected by a moving average smoothing method (moving averaged values = 5). GFP and RFP profiles of sample cells were independently analysed as follows. First, GFP and RFP signals were background and bleaching corrected, using Eq E1 and E2:

$$\boldsymbol{Single-Cell\ GFP/RFP\ profile_{tn}} = \left(\left(Profile\ signal_{tn} - Bckg_{tn}\right)/bleaching\ correction\ coefficient_{\ tn}\right) \quad \text{(E3)}$$

where *Profile signal* intensity represents the GFP or RFP raw profile values across the plasma membrane, *Bckg* stands for the average fluorescence intensity of 6 independent cell-free regions, and t_n represents a given time point along the time course of the experiment.

Corrected single-cell GFP and RFP profiles were then aligned to their peaks in order to correct for cell growth and/or cell movement. The RFP peak at t_0 was used as a reference point to align single-cell RFP and GFP profiles over time. The profiles resulting from the peak alignment were used to calculate the cortical GFP and RFP fluorescence values over time:

$$\boldsymbol{Corticl\ RFP\ Trace_{\ tn}} = \left(RFP\ intensity_{peak-1pixel\ tn} + RFP\ intensity_{peak\ tn} + RFP\ intensity_{peak+1pixel\ tn}\right)/_3 \quad \text{(E4)}$$

$$\boldsymbol{Cortical\ GFP\ Trace_{\ tn}} = \left(GFP\ intensity_{peak-1pixel\ tn} + GFP\ intensity_{peak\ tn} + GFP\ intensity_{peak+1pixel\ tn}\right)/_3 \quad \text{(E5)}$$

The GFP and RFP fluorescence intensities at $RFP_{\text{peak pixel position at t0}} \pm 1$ pixel were averaged in order to extract CRY2PHR-mCherry tip depletion (RFP channel) and GFP-tagged traces across the duration of the time-lapse. From here on, GFP traces were saved and further analyses were

performed only for RFP traces. First, the amplitude of the RFP tip depletion was calculated as follows:

$$\boldsymbol{Amplitude\ RFP\ depletion} = \left(\left(Cortical\ RFP\ Trace_{t0} - average\left(Cortical\ RFP\ Trace_{t13-t18}\right)\right) \Big/ Cortical\ RFP\ Trace_{t1}\right) * 100 \quad \text{(E6)}$$

where *Cortical RFP trace* t_0 represents the initial RFP signal at the plasma membrane and *average* (*Cortical RFP trace* $t_{13\text{-}18}$) represents the average signal at the plasma of the last 5 timepoints of the trace. In addition, single-cell RFP traces derived from Eq E4 were also normalized to their own maximum RFP intensity:

$$\boldsymbol{Max.\ Normalized\ RFP\ trace} = \left(Cortical\ RFP\ Trace_{tn} \Big/ Cortical\ RFP\ Trace_{tmax}\right) \quad \text{(E7)}$$

where *Cortical RFP trace* t_n represents the RFP value of the trace at the timepoint *n* and *Cortical RFP trace* t_{max} represent the maximum RFP value of the single-cell trace.

From here on, normalized RFP traces from Eq E7 were sorted according to the amplitude of depletion derived from Eq E6. When the *Amplitude RFP depletion* was lower than 20 %, then the normalized RFP trace from Eq E7 was labelled as "Non-depleted". These traces are represented in red-coloured dots in Fig 1B and similar cluster plots. Cumulative GFP values of "Non-depleted" RFP traces were calculated as follows:

$$\boldsymbol{GFP\ value}_{\boldsymbol{Non-depleted\ trace}} = Cortical\ GFP\ Trace_{t1} + Cortical\ GFP\ Trace_{t2} \ldots + Cortical\ GFP\ Trace_{tn} \quad \text{(E8)}$$

Where *Cortical GFP trace* t_n represents the GFP value at timepoint n from the GFP trace calculated in Eq E5. Thus, GFP value for "Non-depleted" RFP traces correspond to the sum of GFP values along the 19 timepoints.

In contrast, when the *Amplitude RFP depletion* was greater than 20 %, then the normalized RFP trace from Eq E7 were labelled as "Depleted". These "Depleted" traces were used to calculate the tip depletion half-times:

$$\boldsymbol{Max.\ Normalized\ RFP\ trace\ t_{max}}: t_n\ (y) = a * e^{(-b*tmax:tn)} \quad \text{(E9)}$$

$$\boldsymbol{Tip\ Depletion\ t_{1/2}} = ln(0.5) \Big/ -b \quad \text{(E10)}$$

where *Max. Normalized RFP trace* t_{max}*:*t_n represent the normalized RFP trace from Eq E7 starting from the timepoint of its maximal RFP value (t_{max}) to the last timepoint of the trace (t_n) and t_n represents the last timepoint of the trace. If t_{max} corresponds to t_0, then it means that the tip was depleting from the very beginning of the recording. In contrast, if t_{max} does not corresponds to t_0, then it means that the tip depletion started later on. Therefore, a *Depletion delay* variable was also calculated.

$$\boldsymbol{Tip\ Depletion\ delay} = t_{max} - t_0 \quad \text{(E11)}$$

where t_{max} represents the timepoint at which the maximal RFP value was detected along the single-cell trace and t_0 represents the first timepoint of the trace. 67% of traces started depleting from t_0, 19% from t_1 and a few % thereafter.

Finally, cumulative GFP values for "Depleted" RFP traces were calculated as follows:

$$\boldsymbol{GFP\ value}_{\boldsymbol{Depleted\ trace}} = Cortical\ GFP\ Trace_{tmax} + Cortical\ GFP\ Trace_{tmax+1} \ldots + Cortical\ GFP\ Trace_{tn} \quad \text{(E12)}$$

where *Cortical trace* t_{max} represents the GFP value of the GFP trace calculated in Eq E5 at timepoint t_{max}. Thus, GFP value for "Depleted" RFP traces correspond to the sum of GFP values from t_{max} to t_n (*n = 19 timepoints*).

After these data analyses, RFP traces were further sorted based on the R^2 value of the fitting from Eq E9 and the *Tip depletion delay* value from Eq E11. "Depleted" RFP traces matching any of these criteria were discarded from the regression analysis:

1) The depletion delay from Eq E11 is more than 90 s (starts depleting after t7).
2) R^2 of curve fitting from Eq E9 is lower than 0.7, except in *ypt3-i5* and LatA experiments, where $R^2 > 0.5$ was accepted.

Additionally, "non-depleted" RFP traces, which depleted less than 20% but initiated depletion after t14 (delay from Eq E11 is more than 200 s) were discarded, as these may represent tips that may in fact eventually deplete, after the time of the time-lapse.

Finally, the cumulative GFP values from Eq E8 and Eq E12 and the amplitude of RFP depletion from Eq E6 of non-depleted and depleted traces were used to perform a linear regression analysis. The linear regression was performed using the correlation matrix scatterplot function for MatLab developed by John Chow* (*82*).

Statistical analyses shown in Fig 1C-D-E and Fig S1G-H were performed by comparing the 2nd quintiles (20% - 40% of GFP signal) of control and treated samples using Kruskal-Wallis test. Quintiles were defined based on GFP intensities of control and treated samples. The range of GFP values within an experiment used to define quintiles was set by the lowest and highest GFP values amongst control and treated samples.

CRY2PHR-mCherry lateral peak formation.

The lateral accumulation of CRY2PHR-mCherry at the edges of the depletion zone at cell tips in a strain co-expressing CRIB-3GFP and the CRY2-CIB1 system (N = 3, n = 268 traces in 134 cells) was monitored by recording the RFP and GFP fluorescence profiles over an ROI that was 3-pixels wide by more than 171-pixels long (≈ 0.25 µm by 14.2 µm) drawn along the cortex of sample cells, as shown by the blue arrow on the scheme on the right. The ROI was drawn from one cell side towards the other cell side, passing across the tip of the cell. The lateral accumulation of CRY2PHR-mCherry at the edges of the depletion zone at cell division site was monitored in the same strain (N = 3, n = 36 traces in 18 ROIs) by recording the RFP and GFP fluorescence profiles over an ROI that was 3-pixels wide by more than 60-pixels long (≈ 0.25 µm by 5 µm) drawn along the cortex of sample cells. The RFP and GFP fluoresce profiles were recorded over time from sample strains. The GFP signal was used to align single-cell RFP and GFP profiles. Because CRY2PHR only achieves its maximal plasma membrane recruitment at the second image acquisition, this was set as t = 0 s. (see Fig 3B).

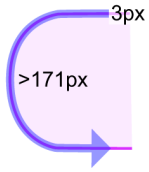

Photobleaching correction coefficients were derived as in Eq E1-E2 and single-cell RFP and GFP cortical profiles were corrected using Eq E3. Single-cell cortical GFP profiles from all the timepoints (*n = 20 timepoints*) were averaged in order to generate an *average Cortical GFP profile.* The peak of the *average Cortical GFP profile* was used as a reference for the center of the cell tip. The peak pixel position of the *average Cortical GFP profile* was fitted to a Gaussian distribution, where the parameter *b* corresponds to the peak position:

$$\boldsymbol{GFP\ Gaussian\ fit}\ (\boldsymbol{y}) = a * e^{-(x-b)^2/2\sigma^2} \quad \text{(E13)}$$

Finally, all single-cell GFP and RFP profiles were aligned to the center of the cell tip, divided symmetrically in two traces and averaged per timepoint (Fig 3B, bottom).

Tip depletion and cell-side accumulation traces were calculated from *single-cell RFP profiles* by averaging the RFP intensities at pixel positions shown in Fig 3B (bottom) for every timepoint. For each cell the average fluorescence value at the cell tip (sampled over 15-pixel length = 1.25 µm), showing depletion over time, and at the edge of the depletion zone (sampled over 10-pixel length = 0.83 µm), showing accumulation over time, was calculated. Average traces are shown in Fig 3B (top).

Cortical distribution profiles of exocytosis (Exo70-GFP) and endocytosis (Fim1-mCherry) at the cell tips and cell middle.

To experimentally address the relative distribution of endo- and exocytosis, we compared the distribution of the exocyst subunit Exo70 and the actin-binding Fimbrin Fim1, as markers of exo- and endocytic events, respectively (*76, 83-85*). Both markers are enriched at cell poles and division sites, and we examined their distribution at both locations (Fig S3). The distribution profiles were generated from the sum projection images of entire time-lapses (n = 21 timepoints). Exo70-GFP and Fim1-mCherry fluorescence profiles were recorded over ROIs drawn from one cortical cell side towards the other cell side (N = 3, n = 149 profiles) and at the cell middle cortex (N = 3, n = 70 profiles) (see Fig S3A and S3B). ROIs were 6-pixel wide by more than 171-pixel long (≈ 0.5 µm by 14.2 µm) for cell tips and 6-pixel wide by 92-pixel long (≈ 0.5 µm by 7.64 µm) for the cell middle.

Single cell profiles were first corrected for the background signal using Eq E14 and E15.

$$\boldsymbol{RFP\ corrected\ profile} = (RFP\ raw\ profile - Bckg_{RFP}) \quad \text{(E14)}$$

$$\boldsymbol{GFP\ corrected\ profile} = (GFP\ raw\ profile - Bckg_{GFP}) \quad \text{(E15)}$$

where *RFP/GFP raw profile* stands for Exo70-GFP and Fim1-mCherry profiles generated from ROIs drawn at cell cortex; and $Bckg_{RFP/GFP}$ stand for the average fluorescence intensity of 6 independent cytosolic regions. $Bckg_{RFP/GFP}$ serve to set fluorescence threshold present in the cytosol of Exo70-GFP and Fim1-mCherry cells. Due to the ubiquitous Fim1-mCherry cortical localization and GFP auto-fluorescence, *Bckg* ROIs were placed in the interception between the nucleus and the cytosol in the centre of cells co-expressing both markers. Upon background correction, RFP and GFP profile values below the threshold (i.e. < 0 A.U.) were set to 0 A.U. in order to prevent numerical aberrations during the analysis.

Single-cell *corrected GFP/RFP profiles* were then normalized to their maximum and minimum values and fitted to a Gaussian distribution using Eq E13. Finally, single-cell *corrected GFP/RFP profiles* were aligned to their geometrical center, averaged and normalized to the maximum and 0 values (Fig S3).

We note that Exo70-GFP exhibits a narrower distribution than Fim1-mCherry at growing cell poles (Fig S3A). We observed similar, even more extensive distribution differences in the middle of pre-divisional cells (Fig S3B). These observations show that endocytosis occurs in a region centred over, but wider than, the zone of polarized exocytosis. These findings are in line with previous observations in several fungi (*86-89*). The measured distributions at cell poles were used in the simulations.

Estimating endocytic and exocytic rates.

To estimate the rate of endocytosis, we counted the number of Fim1-mCherry patches at the cell side of cells co-expressing Exo70-GFP and Fim1-mCherry markers across the duration of the whole time-lapse. We also measured the average fluorescence intensity over the same cell-side regions in sum intensity projection images. These values were used to calculate an average Fim1-mCherry patch fluorescence. We performed this analysis at cell sides rather than cell tips to avoid overlap of endocytic signal at cell tips due to high density, which would lead to an underestimation of the number of events. By dividing the Fim1-mCherry distribution profile described above by the average patch fluorescence value, the average endocytic rate per pixel position across the Fim1-mCherry distribution profile was calculated as follows:

$$\boldsymbol{Endocytic\ rate_n} = ((^{(Mean\ Fim1-mCherry\ fluo._n/mean\ patch\ fluo.)}/_{21}) * 4) * 0.75 \qquad \text{(E16)}$$

where *Mean Fim1-mCherry fluo.* $_n$ stands for the average RFP fluorescence value at pixel position n; *mean patch fluo.* stands for the average Fim1-mCherry patch fluorescence. The value 21 represents the number of time points that contribute to the average Fim1-mCherry distribution profile. This division aims to estimate the number of endocytic event per image. This is multiplied by 4 to obtain the number of events per minute (imaging interval = 15s). Finally, the result of this operation was corrected by 0.75 in order to correct for the slight over sampling in our images, as the average lifetime of a Fim1-mCherry patch is about 20 s (*85*).

The rate of exocytosis events under growth conditions was calculated from the addition of the above rates of endocytosis and rates membrane addition contributing to cell growth. Cell growth was measured in time-lapse imaging as the difference in length over time between the invariant birth scar location and the pole of the cell, and converted to amount of required membrane to accommodate this growth (see model methods for further details).

The obtained values were used in the simulations and are presented in Table 1.

Cortical distribution profiles of GFP-1RitC, GFP-2RitC, GFP-3RitC and 3GFP-1RitC.

Strains co-expressing CRIB-3mCherry and any of the GFP-1RitC (N = 3, n = 266 profiles), GFP-2RitC (N = 3, n = 194 profiles), GFP-3RitC (N = 3, n = 246 profiles) or 3GFP-1RitC (N = 3, n = 274 profiles) constructs were imaged. Cortical distribution profiles were generated from single timepoint middle section images. The RFP and GFP fluorescence profiles were recorded over an ROI that was 3-pixels wide by more than 171-pixels long (≈ 0.25 µm by 14.2 µm) drawn along the cortex of sample cells. The ROI was drawn from one cell side towards the other cell side, passing across the tip of the cell. To correct single-cell profiles for the average camera background signals (*Bckg*), the average signal from 6 cell-free regions was subtracted using Eq E14 and E15. Single-cell *corrected GFP/RFP profiles* were then aligned to their geometrical center and divided symmetrically in two traces starting from the cell pole. To normalize for the differential plasma membrane binding affinity of the GFP-1RitC, GFP-2RitC, GFP-3RitC or 3GFP-1RitC constructs, and compare fluorescence distribution, the area under the curve (AUC) of single-cell *corrected GFP traces* were normalized to 1:

$$\boldsymbol{Normalized\ GFP\ trace} = Corrected\ GFP\ trace/AUC_{trace} \qquad \text{(E17)}$$

where *Corrected GFP trace* represents the fluorescence profile from the cell pole after background correction and AUC_{trace} stands for its area under the curve. Finally, *normalized GFP traces* were averaged (Fig 3E).

For the quantification of tip to side fluorescence intensities of the RitC series (Fig 4E) and correlation to CRIB-3xmCherry (Fig S6), 7 px-wide lines were drawn, one 12 px-long at the tip and two covering the cell sides to measure an average fluorescence signal at cell tip and at cell sides, respectively. Background corrections from the average value of 6 ROIs outside any cell from each individual field of view were performed for each channel. Tip/side ratios were calculated and plotted against CRIB intensity as scatter plots, with R^2 value calculated from the trend line generated in Excel. Data was collected from three replicate experiments for a total of 100-180 cells per strain.

Distribution profile of Rga4 and Rga4 fragments

For the corset profiles of Rga4 in Fig 5A, a 7 px-wide line was drawn along the cell cortex starting from the cell tip with higher CRIB intensity on a sum projection image obtained from z-stack AiryScan acquisition. Background correction from the average value of 6 ROIs in regions outside cells from each individual field of view was performed.

Cortical profiles for Rga4 fragments (Fig 5F) were manually drawn as 7px-wide cortical lines from cell tip to cell tip along each side of the cell and data was collected using the ImageJ multi-plot function. The middle of each profile was identified, the profiles were split in half and aligned to cell tips using MatLab. Background correction from the average value of 6 ROIs outside of cells from each individual field of view was performed. The plots represent data from three replicate experiments with a total of 150-180 cells per strain, shaded area is standard deviation between cells.

TIRF movies were analysed using the TrackMate Fiji plug-in (*90*) and tracking was performed on individual cells. The particle diameter was set to 0.3 µm with maximum gap linking of two frames, and linking range of 0.15 µm. Quality control for spot identification was set at cut-off of 19 and was visually confirmed for each movie.

All boxplots and violin plots were generated using the BoxPlotR web-tool (http://shiny.chemgrid.org/boxplotr/) with definition of whisker extend by Tukey.

Analysis of optoGAP

The quantification of optoGAP and no GAP in Fig 6E shows the number of cells with a clear CRIB zone divided by the total number of cells in both light and dark condition. Quantifications were performed from 3 replicate experiments with a total number of counted cells indicated in the figure. Error bars represent standard deviation between experiments. The CRIB fluorescence intensity profile in Fig 6C was quantified by drawing, for each cell with a CRIB zone, two 7 px-wide profiles along the cell cortex starting at the middle of the cell tip. Data was collected using the multi-plot function of ImageJ and corrected for background from ROIs outside of cells for each individual field of view. For the *rga3*Δ *rga4*Δ *rga6*Δ cells without transgene, only cells with a single CRIB zone were considered. Data was collected from three replicate experiments for a total of 150 cells per strain. Shaded area represents standard deviation between cells. The aspect ratio in Fig 6D was calculated from the measured cell length to cell width of dividing cells in three replicate calcofluor experiments for 500-600 cells per strain. Statistics were performed on the averages of the three experiments using a student t-test with equal variances in Microsoft Excel.

Cortical kymographs

Kymographs shown in Fig 3C and Fig S3 were generated with the MultipleKymograph (https://www.embl.de/eamnet/html/body_kymograph.html) ImageJ plugin using a 1-pixel-wide and 6-pixel-wide ROI drawn along the cell cortex, respectively. Kymographs in Fig 6G-H were generated with the FIJI stack > reslice tool without interpolation using a static 15-pixel-wide segmented line drawn along the cell cortex.

Table S1: *S. pombe* strains used in this study

Number	Genotype	Source
	Fig 1, Fig S1, Fig S3	
YSM3568	*h- leu1-32::Ppak1-CRIB-3xGFP-KanMX+:leu1+ ura4-D18::Ptdh1-CIBN-mTagBFP2-Ritc-ADH1term-Pact1-CRY2PHR-mCherry:ura4+ ade6+ leu1-32*	(*2*)
YSM3564	*ura4-294::Pact1-CRY2PHR-mCherry::ura4+ ade6+ leu1+ ura4-294*	(*2*)
YSM3803	*h- ade6-D19::pnmt41-GFP-ypt3-hph+::Ade6+ ura4-D18::Ptdh1-CIBN-mTagBFP2-Ritc-ADH1term-Pact1-CRY2PHR-mCherry:ura4+ ade6- leu1+ ura4-D18*	This study.
YSM3801	*exo70-GFP-Kan+ ura4-::Ptdh1-CIBN-mTagBFP2-RitC-Adh1term-Pact1-CRY2PHR-mCherry::ura4+ ade6+ leu1+ ura4-*	This study.
YSM3802	*exo84-GFP-Kan+ ura4-::Ptdh1-CIBN-mTagBFP2-RitC-Adh1term-Pact1-CRY2PHR-mCherry:ura4+ ade6+ leu1+ ura4-*	This study.
YSM3807	*h- fim1-mCherry-Nat+ exo70-GFP-Kan+ ade6+ leu1+ ura4+*	This study.
YSM3809	*ypt3-I5(ts) leu1-32::CRIB-3GFP-Kan+::leu1+ ura4-::Ptdh1-CIBN-mTagBFP2-RitC-Adh1term-Pact1-CRY2PHR-mCherry::ura4+ ade6+ leu1-32 ura4-*	This study.
YSM3808	*sty1::bsd leu1-32::CRIB-3GFP-kanMX-leu+ ura4-::Ptdh1-CIBN-mTagBFP2-RitC-Adh1term-Pact1-CRY2PHR-mCherry::ura4 ade6+ leu1-32 ura4-*	This study.
	Fig 3, Fig S6	
YSM3568	*h- leu1-32::ppak1-CRIB-3xGFP-KanMX+:leu1+ ura4-D18::Ptdh1-CIBN-mTagBFP2-Ritc-ADH1term-pact1-CRY2PHR-mCherry:ura4+ ade6+ leu1-32*	(*2*)
YSM3564	*ura4-294::pact1-CRY2PHR-mCherry::ura4+ ade6+ leu1+ ura4-294*	(*2*)
	Fig 4, Fig S6, S7, Fig S8	
YSM3811	*h- ura4+::pact1:sfGFP-3RitCb:terminatortdh1 ade6-M210 leu+*	This study.
YSM3812	*h- ura4+::pact1:sfGFP-2RitC:terminatortdh1 ade6-M210 leu+*	This study.
YSM3813	*h- ura4+::pact1:sfGFP-1RitC:terminatortdh1 ade6-M210 leu+*	This study.
YSM3814	*h- ura4::pact1-3sfGFP-1RitC-tdhterminator::ura4+ ade6-M210 leu1+*	This study.
YSM3815	*h+ ura4+::pact1:sfGFP-1RitC:terminatortdh1 ade6+::pact1:mCherry-1RitC:termScADH1 leu+*	This study.
YSM3816	*h- ura4+::pact1:sfGFP-2RitC:terminatortdh1 ade6+::pact1:mCherry-1RitC:termScADH1 leu+*	This study.
YSM3817	*h+ ura4+::pact1:sfGFP-3RitCa:terminatortdh1 ade6+::pact1:mCherry-1RitC:termScADH1 leu+*	This study.
YSM3818	*ura4::pact1-3sfGFP-1RitC-tdhterminator ade6+::pact1:mCherry-1RitC:termScADH1 leu1+*	This study.
YSM3819	*ura4+::pact1:sfGFP-1RitC:terminatortdh1 his5+::pact1:CRIB[gic2aa1-181]-3mCherry::bsdMX ade6+ leu1+*	This study.
YSM3820	*ura4+::pact1:sfGFP-2RitC:terminatortdh1 his5+::pact1:CRIB[gic2aa1-181]-3mCherry::bsdMX ade6+ leu1+*	This study.
YSM3821	*ura4+::pact1:sfGFP-3RitCb:terminatortdh1 his5+::pact1:CRIB[gic2aa1-181]-3mCherry::bsdMX ade6+ leu1+*	This study.
YSM3822	*ura4::pact1-3sfGFP-1RitC-tdhterminator::ura4+ his5+::pact1:CRIB[gic2aa1-181]-3mCherry::bsdMX ade6+ leu1+*	This study.
YSM3905	*sty1Δ::kanMX ura4+::pact1:sfGFP-3RitCb:terminatortdh1 his5+::pact1:CRIB[gic2aa1-181]-3mCherry::bsdMX ade6+ leu1+*	This study.
YSM1916	*h+ leu1-32:pact1:LifeAct-GFP:leu1+ leu1- ura4-D18*	(*91*)
	Fig 5, Fig S7, S8	
YSM3823	*ura4-294:pshk1:CRIB-3GFP:ura4+ rga4-RFP:kanMX leu1-32*	This study.
YSM3826	*h+ rga4Δ::kanMX ade6-M210 leu1-32 ura4-D18*	This study.
YSM3827	*h+ rga4Δ::kanMX ura4::pact1-rga4(1-685)-GFP::ura4+ ade6-M210 leu1-32*	This study.
YSM3828	*h+ rga4Δ::kanMX ura4::pact1-rga4(1-623)-GFP:ura4+ ade6-M210 leu1-32*	This study.
YSM3829	*h+ rga4Δ::kanMX ura4::pact1-rga4(1-470)-GFP::ura4+ ade6-M210 leu1-32*	This study.
YSM3830	*h+ rga4Δ::kanMX ura4::pact1-rga4(1-623)-RitC-GFP::ura4+ ade6-M210 leu1-32*	This study.
YSM3831	*h+ rga4Δ::kanMX ura4::pact1-rga4(607-685)-GFP:ura4+ ade6-M210 leu1-32*	This study.
YSM3832	*h+ rga4Δ::kanMX ura4::pact1-rga4(465-685)-GFP::ura4+ ade6-M210 leu1-32*	This study.
YSM3833	*h+ rga4Δ::KanMx ura4-pact1-rga4(465-685-F630A-L633A-L640A)-GFP::ura4+ ade6-M210 leu1-32*	This study.

YSM3834	*h+ rga4Δ::kanMX ura4::pact1-rga4(465-685KR670-1AA; KR675-6AA)-GFP::ura4+ ade6-M210 leu1-32*	This study.
YSM3835	*h+ rga4Δ::kanMX ura4::pact1-rga4(465-685-F630A-L633A-L640A- KR670-1AA; KR675-6AA)-GFP::ura4+ ade6-M210 leu1-32*	This study.
YSM3836	*h+ rga4::kanMX ura4::pact1-rga4(465-666)-GFP::ura4+ ade6-M210 leu1-32*	This study.
YSM1408	*h- rga4-GFP:kanMX ade6+ leu1-32 ura4-D18*	(*29*)
YSM3837	*h- rga4-F630A,-L633A,-L640A-GFP-natMX ade6- leu1- ura4-*	This study.
YSM3838	*h- rga4-KR670/671AA-KR675/676AA-GFP-NAT ade6- leu1- ura4-*	This study.
YSM3839	*h- rga4-F630A,-L633A,-L640A-KR670/671AA,-KR675/676AA-GFP-natMX ade6- leu1- ura4-*	This study.
YSM3840	*rga3Δ::hphMX rga6Δ::kanMX rga4-GFP:kanMX ade6- leu1- ura4-*	This study.
YSM3841	*rga3Δ::hphMX rga6Δ::kanMX rga4-FLL-GFP-kanMX ade6- leu1- ura4-*	This study.
YSM3842	*rga6Δ::kanMX rga3Δ::hphMX rga4-KR670/671AA-KR675/676AA-GFP-natMX ade6- leu1-ura4-*	This study.
YSM3843	*rga6Δ::kanMX rga3Δ::hphMX rga4-F630A,-L633A,-L640A-KR670/671AA,-KR675/676AA-GFP-natMX ade6- leu1- ura4-*	This study.
YSM3844	*h+ rga4Δ::kanMX ura4::pact1-rga4(4x607-685)-GFP:ura4+ ade6-M210 leu1-32*	This study.
YSM3845	*h+ rga4Δ::kanMX ura4::pact1-rga4 (4x465-666)-GFP-ura4+ ade6-M210 leu1-32*	This study.
YSM3846	*h+ rga4Δ::kanMX ura4::pact1-CRY2-mcherry-rga4(607-685)::ura4+ ade6-M210 leu1-32*	This study.
YSM3847	*h+ rga4Δ::kanMX ura4::ppom1-rga4(465-685)-GFP::ura4+ ade6-M210 leu1-32*	This study.
YSM3848	*h+ rga4Δ::kanMX ura4::ppom1-rga4(465-666)-GFP::ura4+ ade6-M210 leu1-32*	This study.
	Fig 6	
YSM3136	*h- rga6Δ::kanMX rga3Δ::hphMX rga4Δ::ura4+ ade6- leu1-*	(*29*)
YSM3907	*h- ade6::pact-CRY2-mCherry-RitC::ade6+ leu1-32::CRIB-3xGFP-kanMX::leu1+ ura4-D18*	This study.
YSM3906	*h- rga3Δ::hphMX rga4Δ::ura4+ rga6Δ::kanMX ade6::pact1-CRY2-mcherry-RitC::ade6+ leu1-32::CRIB-3xGFP-kanMX::leu1+*	This study.
YSM3824	*h- rga3Δ::hphMX rga4Δ::ura4+ rga6Δ::kanMX ade6::pact1-CRY2-mCherry-RitC-rga4GAP::ade6+ leu1-32*	This study.
YSM3825	*h- rga3Δ::hphMX rga4Δ::ura4+ rga6Δ::KanMX ade6::CRY2-mCherry-Ritc-rga4GAP::ade6+ leu1::CRIB-3GFP-KanMX:leu1+*	This study.

Table S2: Plasmids used in this study

Number	Description	Purpose
pAV0327	pUra4AfeI-pact1-sfGFP-terminatortdh1	*ura4* integration
pAV0328	pUra4AfeI-pact1-mCherry-terminatortdh1	*ura4* integration
pAV0356	pAde6$_{PmeI}$	*ade6* integration
pAV0605	pUra4$_{AfeI}$-pact1-sfGFP-1RitC-terminatortdh1	*ura4* integration
pAV0602	pUra4$_{AfeI}$-pact1-sfGFP-2RitC-terminatortdh1	*ura4* integration
pAV0601	pUra4$_{AfeI}$-pact1-sfGFP-3RitC-terminatortdh1	*ura4* integration
pAV0607	pAde6$_{PmeI}$-pact1-mCherry-1RitC-termScAdh1	*ade6* integration
pSM2652	pUra4$_{AfeI}$-pact1-3sfGFP-1RitC-tdhterminator	*ura4* integration
pSM0621	pREP41-GFP	cloning backbone
pSM2672	pUra4$_{AfeI}$-pact1-rga4(aa1-685)-GFP-terminatortdh1	*ura4* integration
pSM2641	pUra4$_{AfeI}$-pact1-rga4(aa1-623)-GFP-terminatortdh1	*ura4* integration
pSM2673	pUra4$_{AfeI}$-pact1-rga4(aa1-470)-GFP-terminatortdh1	*ura4* integration
pSM2642	pUra4$_{AfeI}$-pact1-rga4(aa1-623)-RitC-GFP-terminatortdh1	*ura4* integration
pSM2617	pUra4$_{AfeI}$-pact1-rga4(aa607-685)-GFP-terminatortdh1	*ura4* integration
pSM2381	pUra4$_{AfeI}$-pact1-rga4(aa465-685)-GFP-terminatortdh1	*ura4* integration
pSM2424	pUra4$_{AfeI}$-pact1-rga4(aa465-685-F630A, L633A, L640A)-GFP-terminatortdh1	*ura4* integration
pSM2383	pUra4$_{AfeI}$-pact1-rga4 (aa465-685-KR670-1AA; KR675-6AA)-GFP-terminatortdh1	*ura4* integration
pSM2480	pUra4$_{AfeI}$-pact1-rga4 (aa465-685-F630A, L633A, L640A ;KR670-1AA; KR675-6AA)-GFP-terminatortdh1	*ura4* integration
pSM2382	pUra4$_{AfeI}$-pact1-rga4 (aa465-666)-GFP-terminatortdh1	*ura4* integration
pSM2635	pUra4$_{AfeI}$-pact1-4xrga4(aa607-685)-GFP-terminatortdh1	*ura4* integration
pSM2479	pUra4$_{AfeI}$-pact1-4xrga4(aa465-666)-GFP-terminatortdh1	*ura4* integration
pSM2384	pUra4$_{AfeI}$-ppom1-rga4(aa465-685)-GFP-terminatortdh1	*ura4* integration
pSM2385	pUra4$_{AfeI}$ -ppom1-rga4(aa465-666)-GFP-terminatortdh1	*ura4* integration
pSM2637	pUra4$_{AfeI}$-pact1-CRY2-mcherry-rga4(aa607-685)	*ura4* integration
pSM2919	pAde6$_{PmeI}$-pact1-CRY2-mCherry-RitC	*ade6* integration
pSM2787	pAde6$_{PmeI}$-pact1-CRY2-mCherry-RitC-rga4(aa665-933)	*ade6* integration
pSM1692	pSp72-112bp$_{upstream}$-Rga4$_{ORF}$(F630A, L633A, L640A)-+112bp$_{downstream}$	mutagenesis; target endogenous locus
pSM1421	pSp72-112bp$_{upstream}$-Rga4$_{ORF}$(KR670/671AA : KR675/676AA)-+112bp$_{downstream}$	mutagenesis; target endogenous locus
pSM1694	pSp72-112bp$_{upstream}$-Rga4$_{ORF}$(F630A, L633A, L640A, KR670/671AA : KR675/676AA)-+112bp$_{downstream}$	mutagenesis; target endogenous locus
pAV0046	pJK148-ppak1-Ntermgic2aa2-181-3GFP-KanMX	*leu32* integration
pSM2366	pAde6-Pnmt41-GFP-Ypt3	*ade6* integration

Table S3: Primers used for mutagenesis. Bold residues indicate changes from the wildtype sequence

Number	Mutation	5'-3' sequence
osm2347	rga4 (F630A;L633A)_for	CTCCGCGAGAATCG**GC**TTCGCGT**GC**ACAAATGGTTGCATC
osm2348	rga4 (F630A;L633A)_rev	GATGCAACCATTTGT**GC**ACGCGAA**GC**CGATTCTCGCGGAG
osm2349	rga4 (L640A)_for	AATGGTTGCATCTAGC**GC**TGGATTTAGACCCAAAG
osm2350	rga4 (L640A)_rev	CTTTGGGTCTAAATCCA**GC**GCTAGATGCAACCATT
osm2351	rga4 (KR670/671AA:KR675/676AA)_for	AGAAGTCATTTTCT**GCAGCG**TTTCATTGG**GCAGCA**GATTCTCCT CACAT
osm2352	rga4 (KR670/671AA:KR675/676AA)_rev	ATGTGAGGAGAA**TCTGCT**GCCCAATGAAA**CGCTGC**AGAAAAT GACTTCT

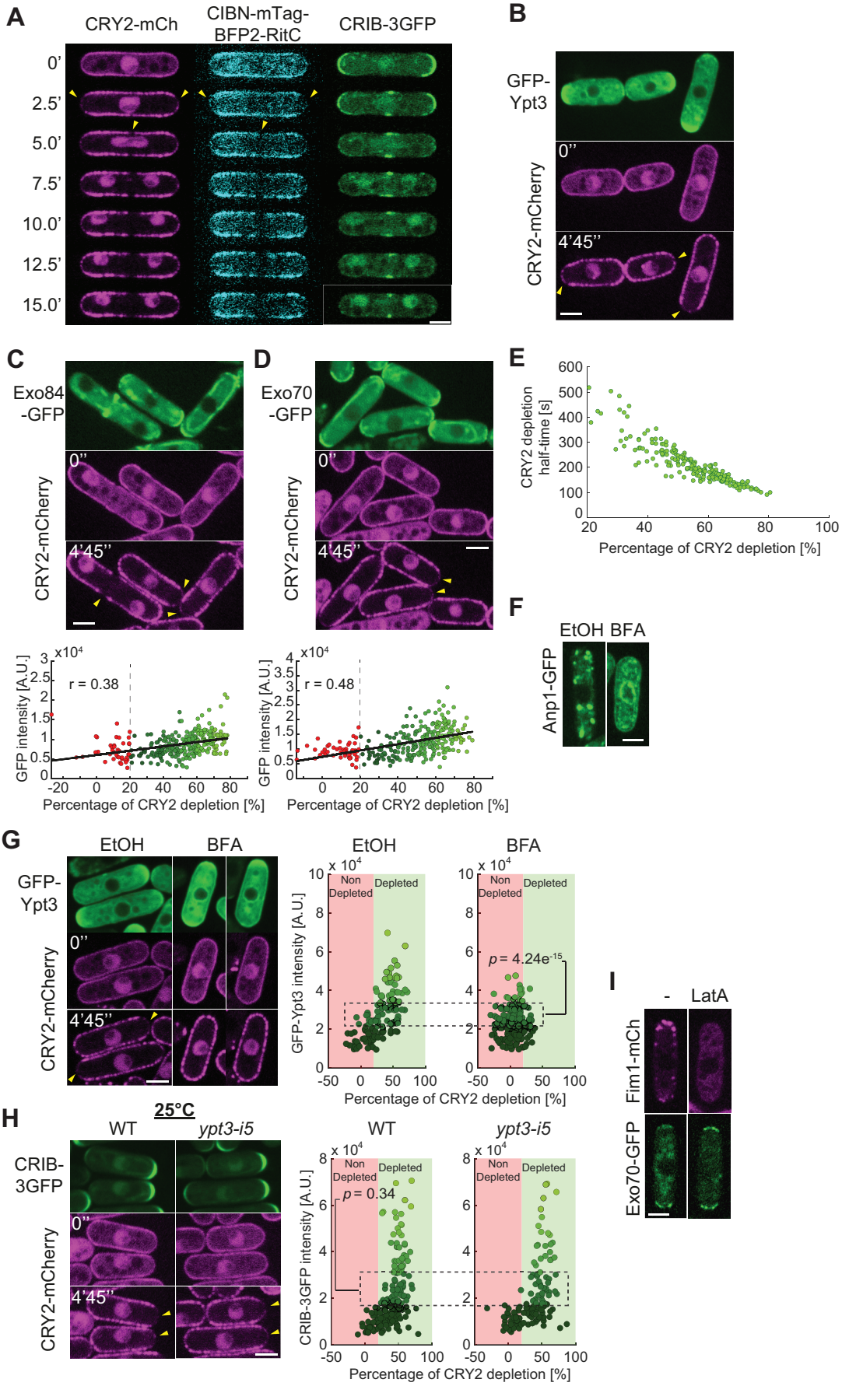
A
CRY2-mCh
CIBN-mTag-BFP2-RitC
CRIB-3GFP
0'
2.5'
5.0'
7.5'
10.0'
12.5'
15.0'
B
GFP-Ypt3
CRY2-mCherry
0''
4'45''
C
Exo84-GFP
CRY2-mCherry
0''
4'45''
GFP intensity [A.U.]
x10^4
r = 0.38
Percentage of CRY2 depletion [%]
D
Exo70-GFP
CRY2-mCherry
0''
4'45''
GFP intensity [A.U.]
x10^4
r = 0.48
Percentage of CRY2 depletion [%]
E
CRY2 depletion half-time [s]
Percentage of CRY2 depletion [%]
F
EtOH BFA
Anp1-GFP
G
EtOH
BFA
GFP-Ypt3
CRY2-mCherry
0''
4'45''
EtOH
BFA
x 10^4
Non Depleted
Depleted
GFP-Ypt3 intensity [A.U.]
p = 4.24e-15
Percentage of CRY2 depletion [%]
H
25°C
WT
ypt3-i5
CRIB-3GFP
CRY2-mCherry
0''
4'45''
WT
ypt3-i5
x 10^4
Non Depleted
Depleted
p = 0.34
CRIB-3GFP intensity [A.U.]
Percentage of CRY2 depletion [%]
I
-
LatA
Fim1-mCh
Exo70-GFP

Figure S1. Controls and further evidence of depletion of membrane-associated CRY2 around sites of secretion

A. Time-lapse of CRY2-mCherry, CIBN-mTag-BFP2-RitC and CRIB-3GFP in a pre-divisional cell grown in the dark. Time 0 is the first timepoint after illumination. Arrowheads point to zones of depletion. **B.** Time-lapse of CRY2-mCherry redistribution in cells co-expressing CIBN-mTag-BFP2-RitC and GFP-Ypt3 (see Fig 1B for quantification). **C-D.** Time-lapse of CRY2-mCherry redistribution in cells co-expressing CIBN-mTag-BFP2-RitC and Exo84-GFP (C) or Exo70-GFP (D). The bottom graph shows correlation between extent of CRY2 depletion after 5 min and pole GFP intensity. In (B-D), cells were grown in the dark. Time 0 is the first timepoint after illumination. The GFP channel is shown as sum projection over the 5 min time-lapse. The mCherry channel shows individual time points. **E.** Correlation between CRY2 depletion halftime and extent of depletion after 5 min. **F.** Example of Anp1-GFP-expressing cells mixed with cells shown in Fig 1C and panel (G), showing the effect of brefeldin A (BFA) on collapse of Golgi to the ER. **G.** Cells as in (B) treated with 50nM brefeldin A (BFA) or solvent (EtOH). **H.** Cells as in Fig 1D, but at 25°C. In (G-H), the GFP channel is shown as sum projection over the 5 min time-lapse. The mCherry channel shows individual time points. Graphs on the right are as in Fig1C-E with depletion cut-off shown in red and green backgrounds. Data points are coloured with different shades of green according to GFP fluorescence levels. The indicated Kruskal-Wallis test *p*-value compares CRY2 depletion values between cells of equivalent CRIB-3GFP intensities. **I.** Example of cell expressing both Fim1-mCherry and Exo70-GFP mixed with cells shown in Fig 1E, showing the effect of Latrunculin A (LatA) on loss of actin patches (but not exocyst localization). Throughout, yellow arrowheads indicate depletion zones. Scale bars are 3µm.

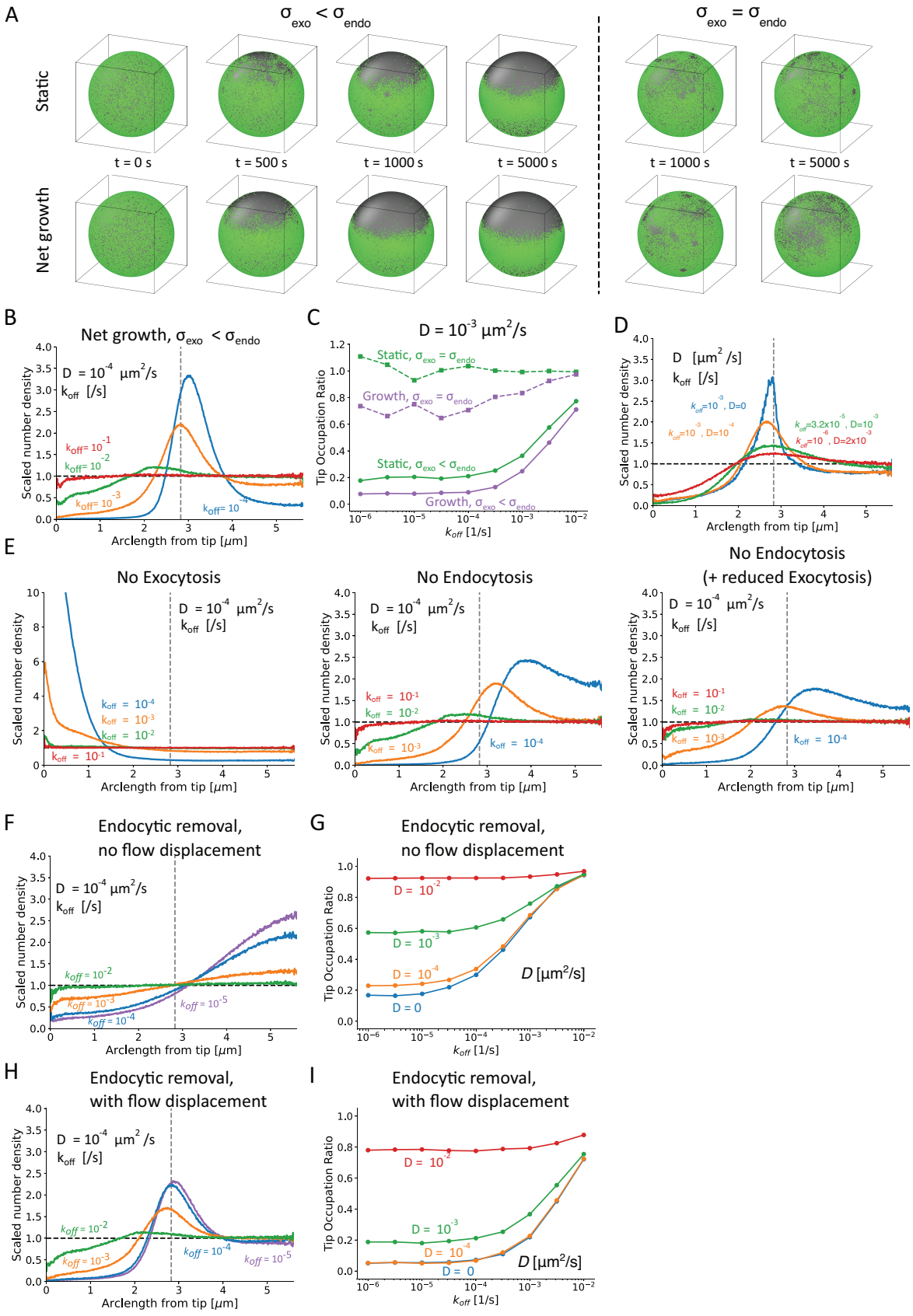
A
σexo < σendo
σexo = σendo
Static
Net growth
t = 0 s
t = 500 s
t = 1000 s
t = 5000 s
t = 1000 s
t = 5000 s
B
Net growth, σexo < σendo
D = 10-4 μm2/s
koff [/s]
koff= 10-1
koff= 10-2
koff= 10-3
koff= 10-4
Scaled number density
Arclength from tip [μm]
C
D = 10-3 μm2/s
Static, σexo = σendo
Growth, σexo = σendo
Static, σexo < σendo
Growth, σexo < σendo
Tip Occupation Ratio
koff [1/s]
D
D [μm2 /s]
koff [/s]
koff=10-3 , D=0
koff=10-3 , D=10-4
koff=3.2x10-5 , D=10-3
koff=10-6 , D=2x10-3
Scaled number density
Arclength from tip [μm]
E
No Exocytosis
No Endocytosis
No Endocytosis
(+ reduced Exocytosis)
D = 10-4 μm2/s
koff [/s]
koff = 10-1
koff = 10-2
koff = 10-3
koff = 10-4
Scaled number density
Arclength from tip [μm]
F
Endocytic removal,
no flow displacement
D = 10-4 μm2/s
koff [/s]
koff = 10-2
koff = 10-3
koff = 10-4
koff = 10-5
Scaled number density
Arclength from tip [μm]
G
Endocytic removal,
no flow displacement
D = 10-2
D = 10-3
D = 10-4
D = 0
D [μm2/s]
Tip Occupation Ratio
koff [1/s]
H
Endocytic removal,
with flow displacement
D = 10-4 μm2 /s
koff [/s]
koff = 10-2
koff = 10-3
koff = 10-4
koff = 10-5
Scaled number density
Arclength from tip [μm]
I
Endocytic removal,
with flow displacement
D = 10-2
D = 10-3
D = 10-4
D = 0
D [μm2/s]
Tip Occupation Ratio
koff [1/s]

Figure S2. Simulation results and conditions for tip depletion and lateral peak.

A. Time evolution of particles (green) on the surface of the sphere with $k_{off} = 10^{-5}/s$ and $D = 10^{-4}\ \mu m^2/s$ under static conditions (top row; net area added is zero with 0.5 endocytosis events/s and 2.44 endocytosis events/s) and under net growth conditions (bottom row; net area added 20.7 $\mu m^2/hr$ with 0.68 exocytosis events/s and 2.44 endocytosis events/s). The spherical shell representing the cell remains at a constant size; exocytosis and endocytosis only affect the positions of particles on the surface. Left: both rows have $\sigma_{exo} = 0.85\ \mu m < \sigma_{endo} = 1.84\ \mu m$ derived from experimental measurements; depletion near the top tip is evident in both cases but occurs faster under growth conditions. Right: both rows have $\sigma_{exo} = \sigma_{endo} = 1.84\ \mu m$; slight depletion near the tip is only evident under growth conditions. **B.** Scaled number density as a function of arclength for the same simulations as Fig 2E but under growth conditions. Compared to Fig 2E, the lateral peak is shifted further towards the back of the sphere and tip depletion is stronger. **C.** Tip occupation ratio as a function of k_{off} for static and growth conditions for $\sigma_{exo} = \sigma_{endo}$ and $\sigma_{exo} < \sigma_{endo}$ as in panel A, for $D = 10^{-3}\ \mu m^2/s$. Switching from $\sigma_{exo} = \sigma_{endo}$ to $\sigma_{exo} < \sigma_{endo}$ or from static to growth conditions both result in increased tip depletion. **D.** Increasing diffusion coefficient while keeping the tip occupancy ratio nearly constant reduces the lateral peak height (net growth, $\sigma_{exo} < \sigma_{endo}$ as in A). **E.** Scaled number density as a function of arclength, for simulations where exocytosis is turned off/endocytosis remains (left); endocytosis is turned off/exocytosis remains the same as under growth conditions (middle); and endocytosis is turned off/exocytosis is reduced so that the net area addition rate is 20.7 $\mu m^2/hr$ (right). Reference parameters are for net growth, $\sigma_{exo} < \sigma_{endo}$ as in (A). Stopping exocytosis leads to tip enhancement for low enough k_{off}. As these simulations do not account for anticipated slowing down of endocytosis due to reduction of plasma membrane lipid reservoir, we consider them consistent with the results of experiments in Fig 1C-D. Stopping endocytosis maintains tip depletion, in line with experiments of Fig 1E. **F.** Scaled number density as a function of arclength at $D = 10^{-4}\ \mu m^2/s$ under no flow displacement conditions where exocytosis/endocytosis does not move the particles on the sphere surface but endocytosis pulls particles into the internal pool if they are within R_{endo} of the endocytosis event (using 2.44 endocytosis events/s and $\sigma_{endo} = 1.84\ \mu m$ as in (A)). Depletion is still evident but the lateral peak near the equator of the sphere disappears. Compare to Fig 2E. **G.** Tip occupation ratio versus k_{off} under no flow displacement conditions as in (F). Tip depletion is less pronounced compared to simulations with displacement in Fig 2D, for the same conditions. **H.** Scaled number density as a function of arclength at $D = 10^{-4}\ \mu m^2/s$ under both flow displacement conditions and endocytosis pulling particles into the internal pool if they are within R_{endo} of the endocytosis event (using 2.44 endocytosis events/s and $\sigma_{endo} = 1.84\ \mu m$ as in (A)). **I.** Tip occupation ratio versus k_{off} under flow displacement conditions and endocytic removal as in (H).

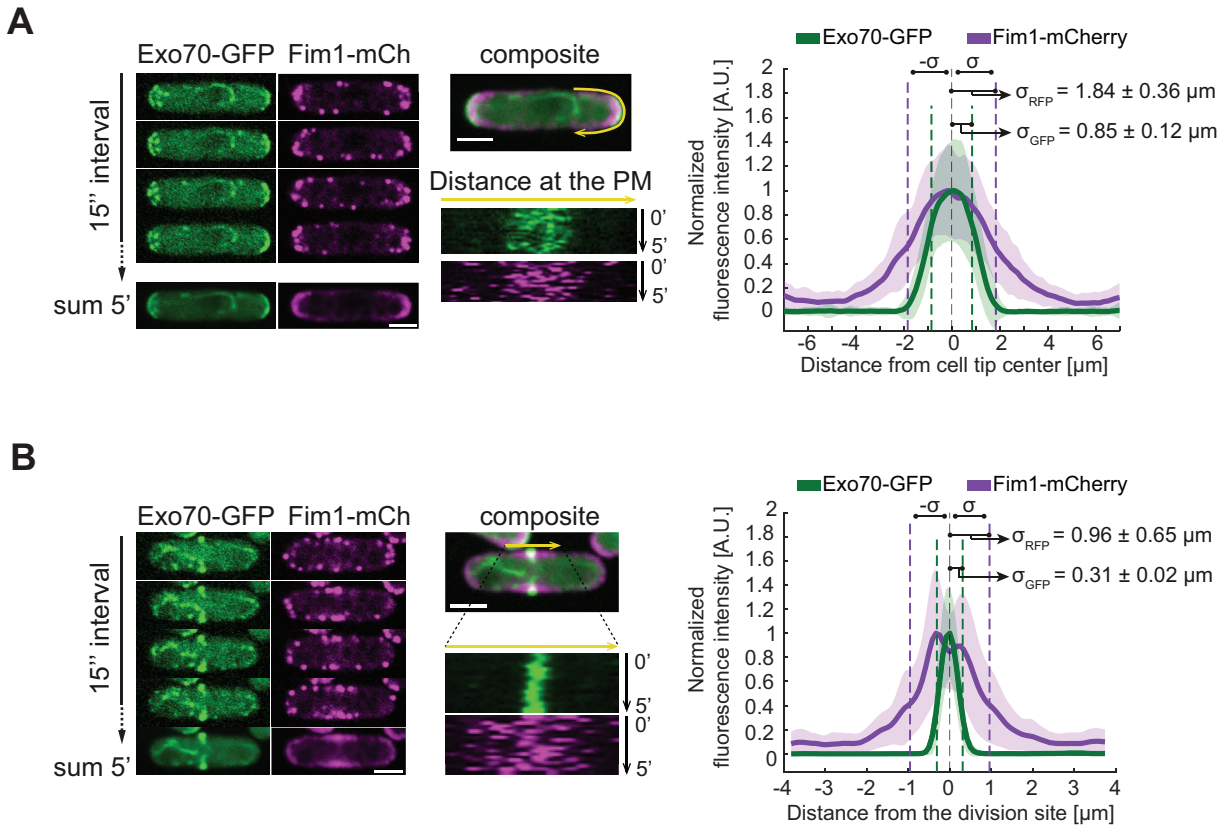

Figure S3. Distribution of exo- and endocytosis in fission yeast cells

A-B. Time-lapse, sum projection and kymographs of the cell pole (A) and the early, pre-constriction division site (B) of cells expressing Exo70-GFP and Fim1-mCherry, marking exo- and endocytic sites, respectively. The graph shows the average distribution of these markers. Shaded areas show standard deviation.

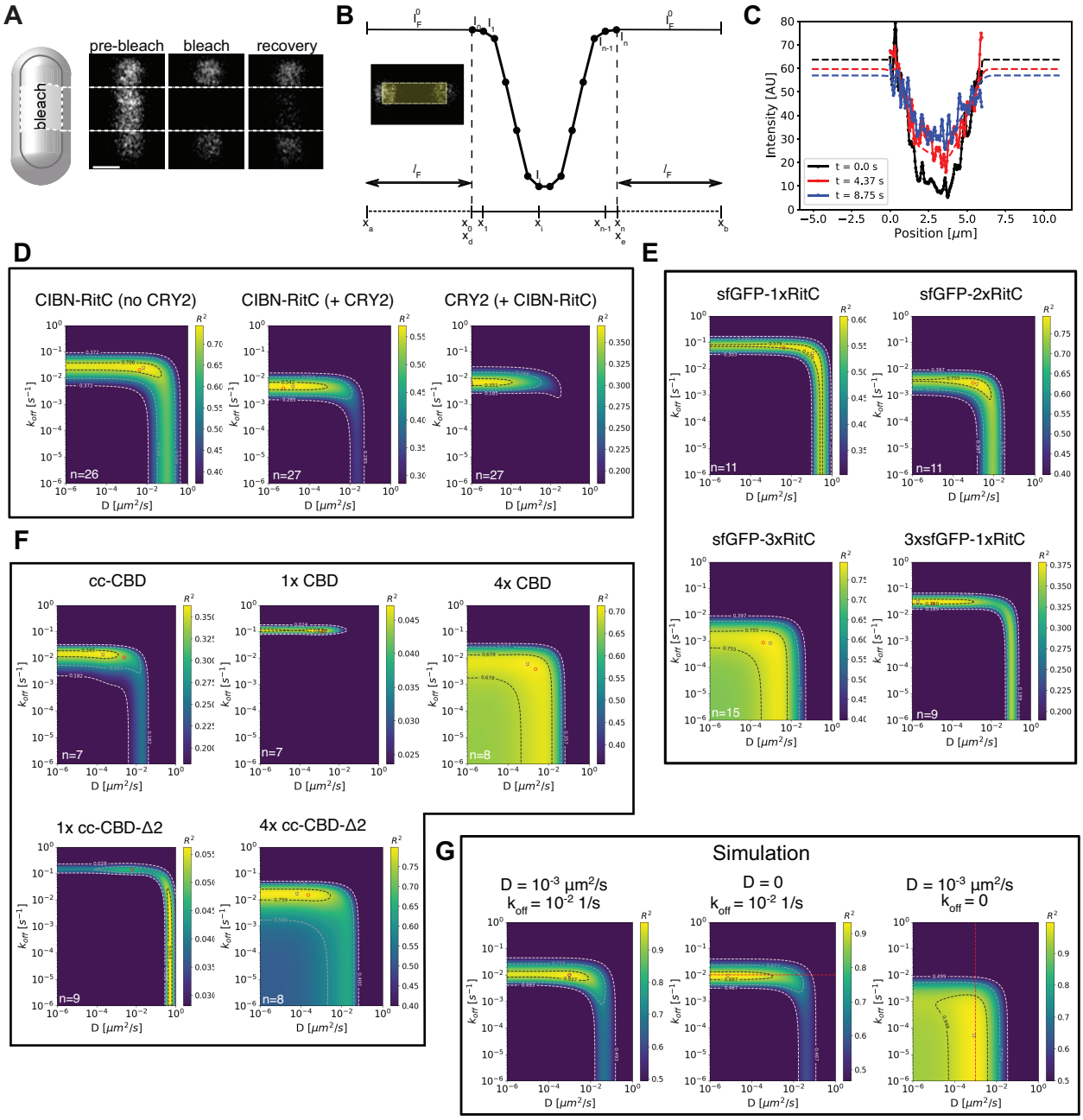

Figure S4. Fitting for diffusion coefficient and membrane dissociation rate with FRAP.

A. A rectangular region along the cylindrical section on one side of the cell was photobleached and the recovery imaged over time. **B.** Schematic of 1D fluorescence recovery model for an experimental profile, extracted by vertical projection along a rectangular region shown in yellow, for the frame after photobleaching ($t = 0$, black circles). The boundaries between the experimentally-sampled middle region and the left and right flanking regions are indicated by dashed vertical lines. **C.** Example recovery curves. Single cell expressing 1xRitC-GFP imaged every 0.729 s and fit using the 1D model over 30 frames. Experimental data shown as lines with filled points while model fits shown as lines without points ($D = 6.85 \times 10^{-3}$ μm$^2/s$, $k_{off} = 0.108\ /s$ and l_F as shown by the end points of the model curves). The black line of the model is

initialized to go through the experimental data points at $t = 0$. **D-F.** Plots of averaged R^2 calculated from FRAP fits for all protein constructs investigated as function of D and k_{off}. Red circles indicate the median of the D and k_{off} values for each protein from individual fits of the 1D model while blue dashed circles indicate the best fit using the average of individual R^2 maps. The number of cells averaged in each plot is indicated by the value of n. **G.** Averaged R^2 plots for simulated FRAP due to both diffusion and membrane binding/unbinding on the surface of a cylinder. Good agreement is found between the input parameters (red circle or dashed line) and the highest value of R^2 (blue circle).

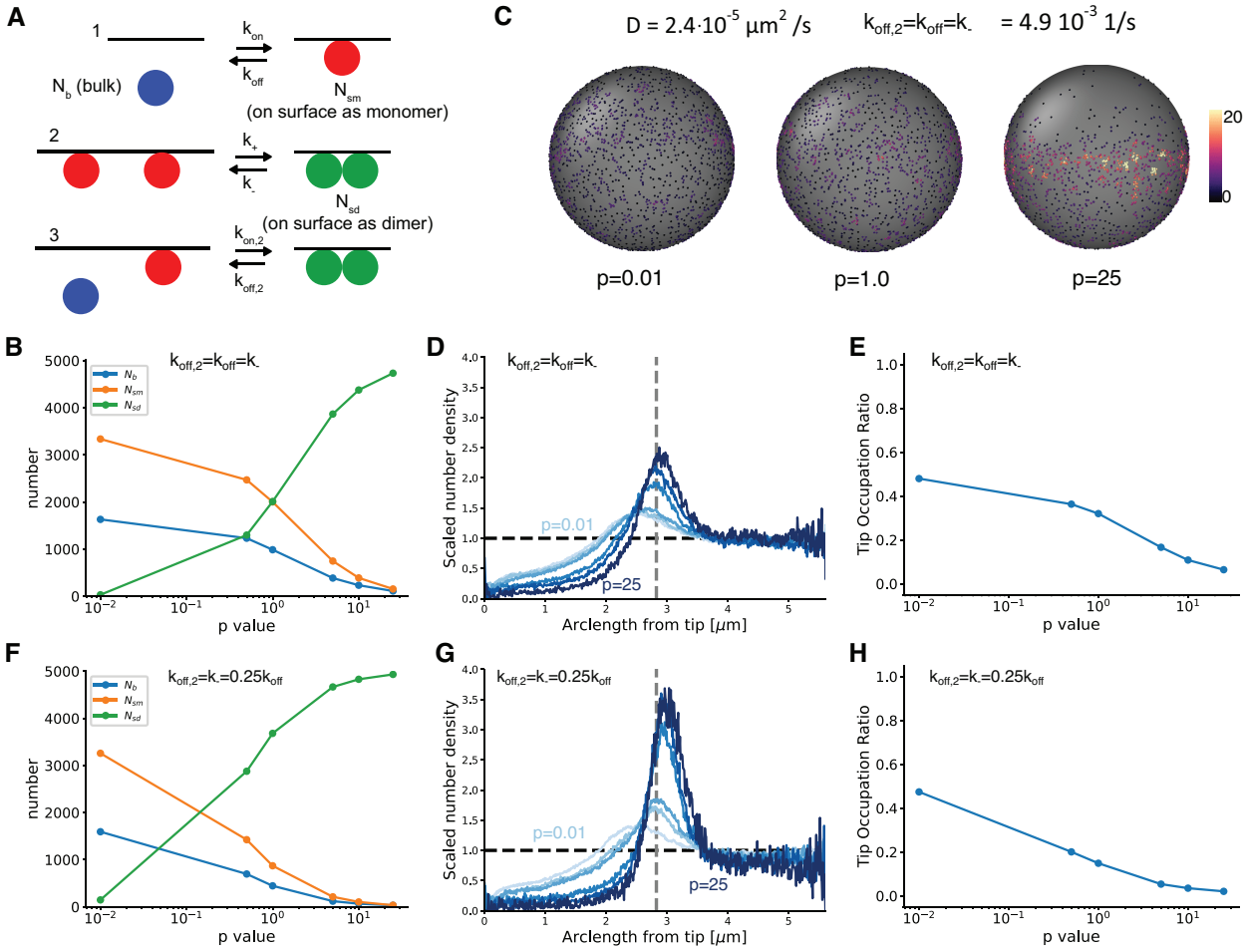

Figure S5. Modified model to include dimer formation on spherical surface, diffusing in the presence of membrane flows.

A. Reactions used in dimerization simulations. The diffusion coefficient of dimers is the same as that of monomers. Reactions obey detailed balance at steady state in absence of endocytic or exocytic flow. **B.** Plots of the number of average particles at steady state as a function of parameter p. Simulations in this and panels D and E have 5000 particles and rate constants as described in methods. **C.** Snapshots of spheres with increasing p value show that tip depletion and lateral concentration increase with increasing p. Color scale shows local density. **D.** Scaled number density of particles as a function of arclength show a similar trend where depletion and lateral peak increase with increasing p. **E.** Tip occupation ratio also decreases as a function of p. **F.** Plots of the number of average particles at steady state as a function of parameter p. Simulations in this and panels G and H have 5000 particles and dimer off rates ($k_{off,2}$ and k_-) equal to a quarter of the single particle off rate (k_{off}). **G.** Scaled number density of particles as a function of arclength have an enhanced depletion and lateral peak compared to panel D. **H.** Tip occupation ratio is slightly decreased compared to panel E.

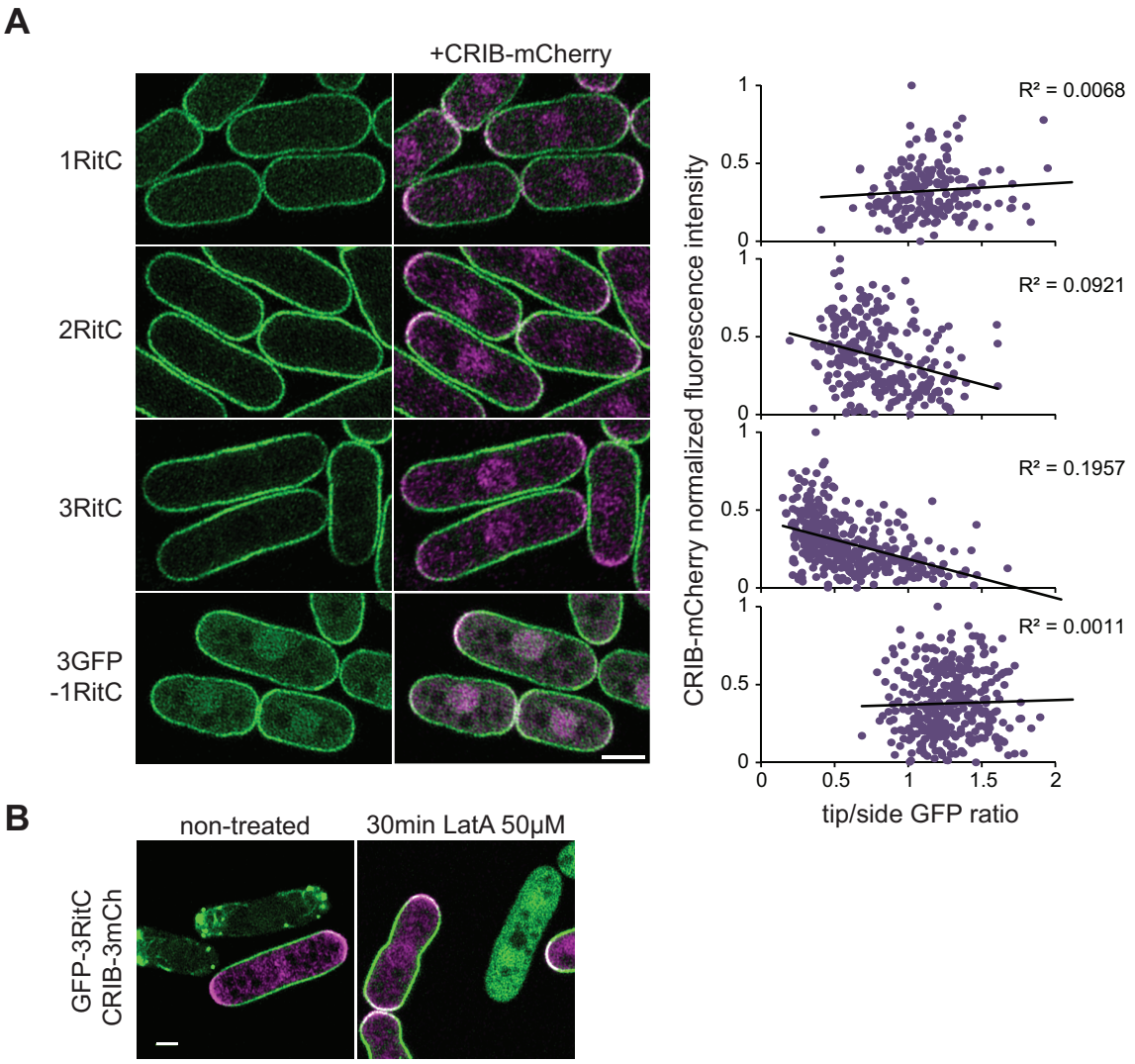

Figure S6. Membrane affinity-dependent depletion of membrane-associated RitC at sites of polarized secretion.

A. Localization of indicated sfGFP-tagged RitC constructs in cells co-expressing CRIB-mCherry. The graphs on the right show correlation plots between the ratio of the tip to side GFP signal and the CRIB-mCherry tip intensity. Note the progressive shift towards the left of the data points upon RitC multimerization, as well as the more marked negative correlation. **B.** sfGFP-3xRitC and CRIB-3xmCherry in *sty1*Δ cells non-treated or treated with LatA for 30min. The cells were mixed with LifeAct-GFP expressing cells as control, showing actin depolymerization upon LatA treatment.

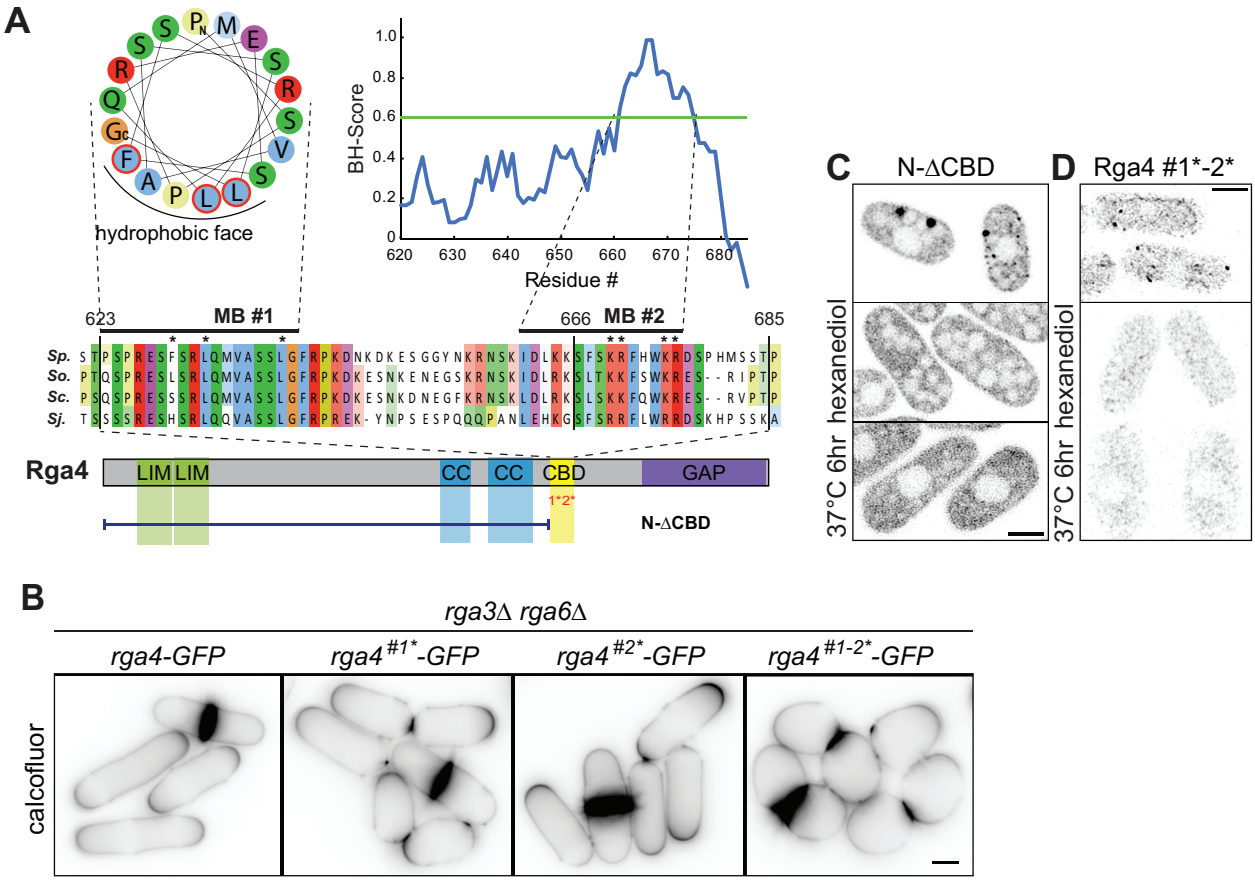

Figure S7. Structure-function analysis of the Cdc42 GAP Rga4 defining membrane-binding and oligomerization motifs

A. Scheme of Rga4 and truncation fragments. The sequence alignment shows the CBD across *Schizosaccharomyces* species (*S.p. = S. pombe*; *S.o. = S. octosporus*; *S.c. = S. cryophilus*; *S. j. = S. japonicus*). Membrane-binding (MB) motif 1 shows a weak amphipathic helix prediction, of which three hydrophobic residues (FLL, red circles and asterisks) were mutated to alanine. MB motif 2 was identified to have a high basic and hydrophobic (BH) scale, predictive of membrane association (*28*). Asterisks highlight four basic residues (KRKR) that were mutated to alanine. **B.** Shape of *rga3Δ rga6Δ* double mutant cells with indicated *rga4* alleles shown by calcofluor imaging. **C.** Dissolution of cytosolic condensates of Rga4 N-terminus lacking the CBD (N-ΔCBD) upon treatment with 10% 1,6-hexanediol or 37°C. **D.** Cytosolic condensates of full-length Rga4 with mutations in MB #1 and #2 are dissolved upon treatment with 5% 1,6-hexanediol or 37°C.

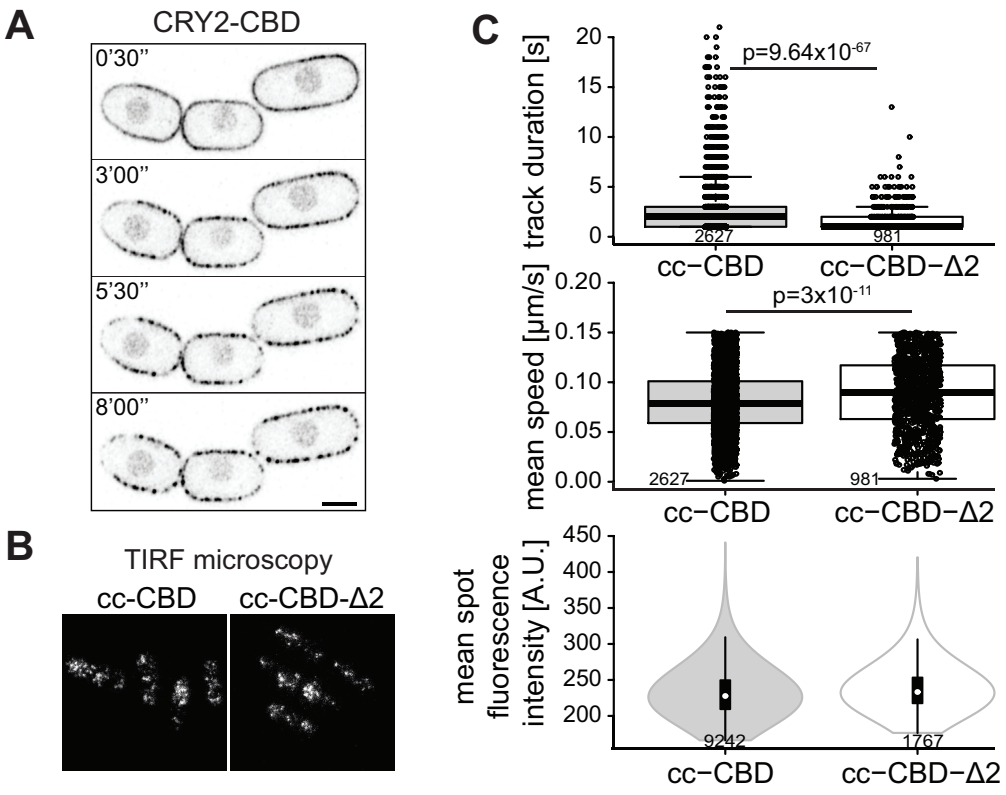

Figure S8. Further characterization of minimal Rga4 fragments

A. Localization of CRY2-CBD in cells grown in the dark and illuminated at time 0. **B.** Localization of cc-CBD and cc-CBD-Δ2 Rga4 fragments by TIRF-microscopy. See Movies 6-7 for time-lapse imaging and cluster tracking. **C.** Quantification of track duration, speed and fluorescence intensity for clusters of Rga4 fragment as in (B). The track duration of cc-CBD-Δ2 clusters was significantly reduced, while their speed was significantly increased, consistent with shorter membrane residence time and faster lateral diffusion. The track duration times and diffusion coefficient implied by the measurements (displacement per time step $\approx (4Dt)^{1/2}$) are in the same range as the median k_{off} and *D* of the FRAP fits in Fig S4F. p-values calculated from student t-test with unequal variances. The fluorescence intensity per cluster was not altered, suggesting unchanged oligomerization properties, as predicted from truncation of the membrane-binding region.

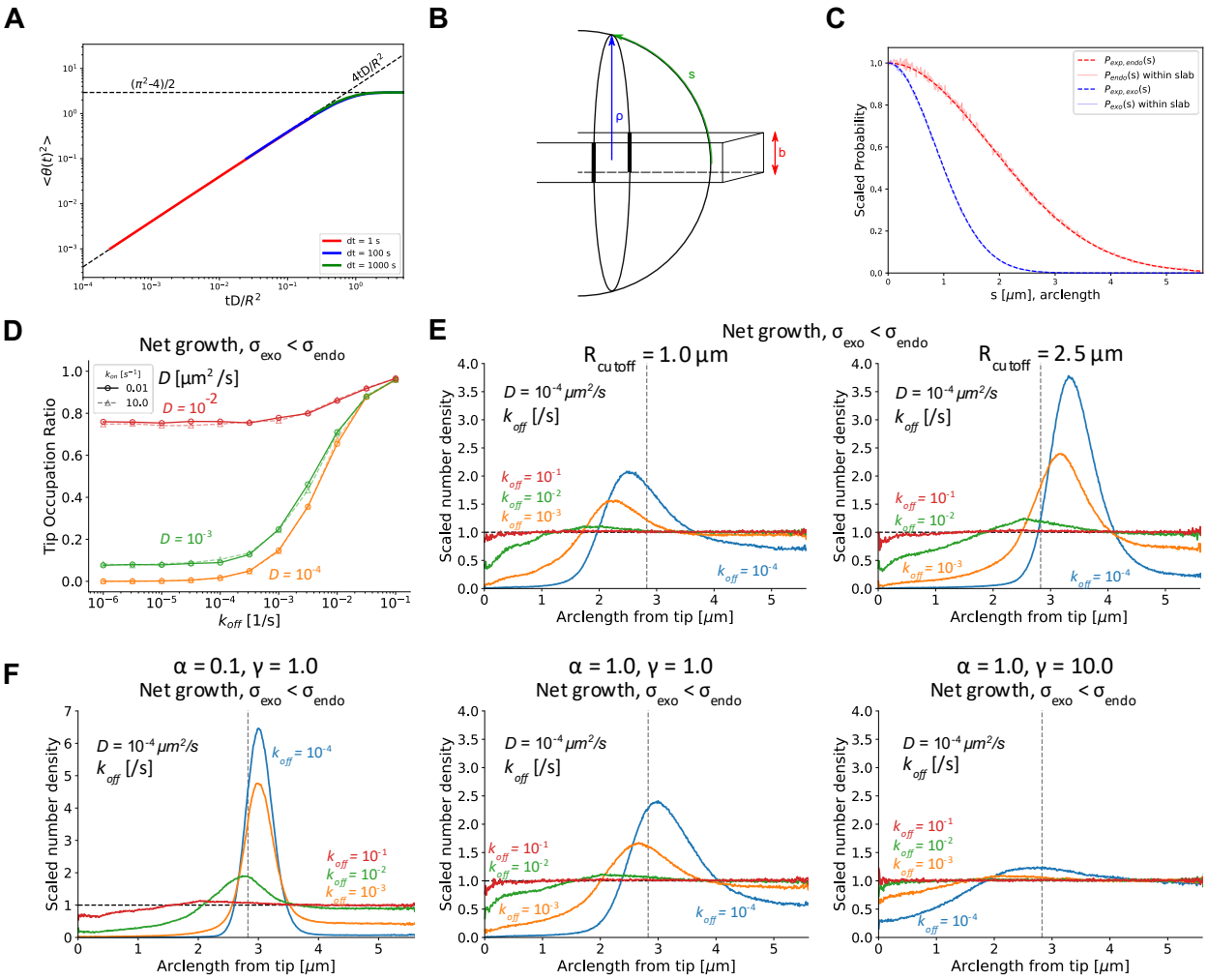

Figure S9. Model calibration and dependence on parameters k_{on}, α, R_{cutoff}, γ.

A. Test of implementation of diffusion on a sphere. Change in polar angle due to diffusion maintains the correct scaling of particle displacement over time, regardless of the timestep. Colored curves show results of averaged mean squared polar angle displacement (in radians squared) for particles diffusing on a sphere with $D = 10^{-3}$ μm$^2/s$, $R = 2$ μm. Dashed lines show asymptotic limits at short and long times from (*55*). The colored curves overlap, each starting from the smallest time, $t = dt$. **B.** Limited vertical resolution of microscope, b, leads to varying fractions of the cell surface being observed at a given arc length, s. **C.** Test of Equation (4): if only events in a slab of height b are counted, sampling in 3D from $P(s)$ recovers the experimentally observed probability distribution, $P_{exp}(s)$, for both the endocytosis and exocytosis profiles. **D.** Varying k_{on} has no effect on the tip occupation ratio over the range of D and k_{off} investigated, as expected. **E.** Lower (higher) values of the cutoff range of exocytosis/endocytosis, R_{cutoff}, leads to a reduction (increase) in tip depletion, along with reduction and leftward (increase and rightward) shift of the lateral peak. Other results in this paper used $R_{cutoff} = 2$ μm. **F.** Parameter α (fraction of flowing membrane) affects tip depletion with lower (higher) values of α lead to enhanced (reduced) tip depletion and lateral peak. Other results in this paper used $\alpha = 0.5$. Increasing parameter γ leads to a reduced tip depletion and lateral peak as proteins are less influenced by the flowing lipids.

Movie legends

Movie 1. Depletion of membrane-associated CRY2 at cell poles

Spinning disk microscopy time-lapse of CRY2-mCherry, CIBN-mTag-BFP2-RitC and CRIB-3GFP cells grown in the dark. Time 0 is the first timepoint after illumination. Images are at 30s interval. The UV channel (CIBN-mTagBFP2-RitC) was acquired every 4 timepoints. Depletion is observed at both poles of the three medial cells. Note that cells containing only CRY2-mCherry, which were used for normalization purposes, are also visible. Scale bar is 5µm.

Movie 2. Depletion of membrane-associated CRY2 at division sites

Spinning disk microscopy time-lapse of CRY2-mCherry, CIBN-mTag-BFP2-RitC and CRIB-3GFP cells grown in the dark. Time 0 is the first timepoint after illumination. Images are at 30s interval. The UV channel (CIBN-mTagBFP2-RitC) was acquired every 4 timepoints. Depletion is observed initially at cell poles and then, as cells enter mitosis and prepare for cytokinesis, at mid-cell, concomitant with CRIB-3GFP accumulation. Scale bar is 5µm.

Movie 3. Simulation of membrane-associated protein depletion by membrane flows

Simulation under static conditions (equal rates of membrane delivery by exo- and endocytosis), with $k_{off} = 10^{-5}$/s and $D = 10^{-4}$ µm^2/s showing depletion from the zone of exocytosis on the top of the sphere.

Movie 4. Simulation showing lack of membrane flow-dependent depletion for a protein with fast membrane unbinding rate

Simulation under static conditions (equal rates of membrane delivery by exo- and endocytosis), with $k_{off} = 10^{-2}$/s and $D = 10^{-4}$ µm^2/s showing absence of depletion from the zone of exocytosis on the top of the sphere.

Movie 5. Localization of 3xRitC during the cell growth cycle

Airyscan microscopy time-lapse of sfGFP-3xRitC and CRIB-3xmCherry in cells during mitotic growth. 3xRitC depletes from zones of growth labelled by CRIB at cell poles during interphase and repopulates the cell poles during mitosis when polarized cell growth stops. 3xRitC also transiently depletes from mid-cell, labelled by CRIB in pre-divisional cells until the initiation of septum invagination. White arrowheads show depletion zones. Scalebar is 5µm.

Movie 6. Dynamics of Rga4 cc-CBD fragment in TIRF microscopy

Tracking of cortical clusters of the Rga4 cc-CBD fragment in cells imaged by TIRF microscopy detected by TrackMate ImageJ plugin. Detected clusters are circles. All trajectories are shown.

Movie 7. Dynamics of Rga4 cc-CBD-Δ2 fragment in TIRF

Tracking of cortical clusters of the Rga4 cc-CBD–Δ2 fragment in cells imaged by TIRF microscopy detected by TrackMate ImageJ plugin. Detected clusters are circles. All trajectories are shown.

Movie 8. Light-induced polarity establishment in *rga3*Δ *rga4*Δ *rga6*Δ optoGAP cells – example of monopolar growth

Airyscan microscopy time-lapse of *rga3*Δ *rga4*Δ *rga6*Δ cells expressing CRIB-3GFP and optoGAP grown in the dark and illuminated with blue light from t = 0. OptoGAP, shown in magenta, initially decorates the entire cell periphery, with CRIB absent from the cell cortex. The cells initiate polarized growth, with depletion of optoGAP, and accumulation of CRIB in a restricted zone.

Movie 9. Light-induced polarity establishment in *rga3*Δ *rga4*Δ *rga6*Δ optoGAP cells – example of bipolar growth

Airyscan microscopy time-lapse of *rga3*Δ *rga4*Δ *rga6*Δ cells expressing CRIB-3GFP and optoGAP grown in the dark and illuminated with the blue light from t = 0. OptoGAP, shown in magenta, initially decorates the entire cell periphery, with CRIB absent from the cell cortex. The cells initiate 2 zones of polarized growth, with depletion of optoGAP, accumulation of CRIB in a restricted zone and outgrowth of a tube.

Movie 10. Long-range movement of optoGAP in dividing in *rga3*Δ *rga4*Δ *rga6*Δ cells

Airyscan microscopy time-lapse of *rga3*Δ *rga4*Δ *rga6*Δ cells expressing CRIB-3GFP and optoGAP grown in the light. OptoGAP, shown in magenta, strongly decorates the back of these monopolar cells, with the site of growth indicated by CRIB localization. As cells enter division, growth ceases, CRIB disappears from the cell pole and reappears at the division site. During cell division, optoGAP exhibits long-range movements away from the division site towards the previously growing cell end.

REFERENCES AND NOTES

1. L. Kozubowski, K. Saito, J. M. Johnson, A. S. Howell, T. R. Zyla, D. J. Lew, Symmetry-breaking polarization driven by a Cdc42p GEF-PAK complex. *Curr. Biol.* **18**, 1719–1726 (2008).

2. I. Lamas, L. Merlini, A. Vjestica, V. Vincenzetti, S. G. Martin, Optogenetics reveals Cdc42 local activation by scaffold-mediated positive feedback and Ras GTPase. *PLOS Biol.* **18**, e3000600 (2020).

3. M. Das, T. Drake, D. J. Wiley, P. Buchwald, D. Vavylonis, F. Verde, Oscillatory dynamics of Cdc42 GTPase in the control of polarized growth. *Science* **337**, 239–243 (2012).

4. A. S. Howell, M. Jin, C. F. Wu, T. R. Zyla, T. C. Elston, D. J. Lew, Negative feedback enhances robustness in the yeast polarity establishment circuit. *Cell* **149**, 322–333 (2012).

5. R. Illukkumbura, T. Bland, N. W. Goehring, Patterning and polarization of cells by intracellular flows. *Curr. Opin. Cell Biol.* **62**, 123–134 (2020).

6. M. C. Wigbers, F. Brauns, C. Y. Leung, E. Frey, Flow induced symmetry breaking in a conceptual polarity model. *Cell* **9**, 1524 (2020).

7. G. Grebnev, M. Ntefidou, B. Kost, Secretion and endocytosis in pollen tubes: models of tip growth in the spot light. *Front. Plant Sci.* **8**, 154 (2017).

8. P. Rowghanian, O. Campas, Non-equilibrium membrane homeostasis in expanding cellular domains. *Biophys. J.* **113**, 132–137 (2017).

9. M. S. Bretscher, Endocytosis: Relation to capping and cell locomotion. *Science* **224**, 681–686 (1984).

10. M. Tanaka, T. Kikuchi, H. Uno, K. Okita, T. Kitanishi-Yumura, S. Yumura, Turnover and flow of the cell membrane for cell migration. *Sci. Rep.* **7**, 12970 (2017).

11. P. R. O'Neill, J. A. Castillo-Badillo, X. Meshik, V. Kalyanaraman, K. Melgarejo, N. Gautam, Membrane flow drives an adhesion-independent amoeboid cell migration mode. *Dev. Cell* **46**, 9–22.e4 (2018).

12. S. Gras, E. Jimenez-Ruiz, C. M. Klinger, K. Schneider, A. Klingl, L. Lemgruber, M. Meissner, An endocytic-secretory cycle participates in Toxoplasma gondii in motility. *PLOS Biol.* **17**, e3000060 (2019).

13. J. Dai, M. P. Sheetz, Axon membrane flows from the growth cone to the cell body. *Cell* **83**, 693–701 (1995).

14. F. D. Kelly, P. Nurse, Spatial control of Cdc42 activation determines cell width in fission yeast. *Mol. Biol. Cell* **22**, 3801–3811 (2011).

15. M. Das, D. J. Wiley, S. Medina, H. A. Vincent, M. Larrea, A. Oriolo, F. Verde, Regulation of cell diameter, For3p localization, and cell symmetry by fission yeast Rho-GAP Rga4p. *Mol. Biol. Cell* **18**, 2090–2101 (2007).

16. M. T. Revilla-Guarinos, R. Martin-Garcia, M. A. Villar-Tajadura, M. Estravis, P. M. Coll, P. Perez, Rga6 is a fission yeast Rho GAP involved in Cdc42 regulation of polarized growth. *Mol. Biol. Cell* **27**, 1524–1535 (2016).

17. A. D. Migliori, L. A. Patel, C. Neale, The RIT1 C-terminus associates with lipid bilayers via charge complementarity. *Comput. Biol. Chem.* **91**, 107437 (2021).

18. F. O. Bendezu, V. Vincenzetti, D. Vavylonis, R. Wyss, H. Vogel, S. G. Martin, Spontaneous Cdc42 polarization independent of GDI-mediated extraction and actin-based trafficking. *PLOS Biol.* **13**, e1002097 (2015).

19. B. Onken, H. Wiener, M. R. Philips, E. C. Chang, Compartmentalized signaling of Ras in fission yeast. *Proc. Natl. Acad. Sci. U.S.A.* **103**, 9045–9050 (2006).

20. L. J. Bugaj, A. T. Choksi, C. K. Mesuda, R. S. Kane, D. V. Schaffer, Optogenetic protein clustering and signaling activation in mammalian cells. *Nat. Methods* **10**, 249–252 (2013).

21. T. G. Turi, P. Webster, J. K. Rose, Brefeldin A sensitivity and resistance in Schizosaccharomyces pombe. Isolation of multiple genes conferring resistance. *J. Biol. Chem.* **269**, 24229–24236 (1994).

22. M. Marek, V. Vincenzetti, S. G. Martin, Sterol biosensor reveals LAM-family Ltc1-dependent sterol flow to endosomes upon Arp2/3 inhibition. *J. Cell Biol.* **219**, e202001147 (2020).

23. D. Bonazzi, J. D. Julien, M. Romao, R. Seddiki, M. Piel, A. Boudaoud, N. Minc, Symmetry breaking in spore germination relies on an interplay between polar cap stability and spore wall mechanics. *Dev. Cell* **28**, 534–546 (2014).

24. D. R. Mutavchiev, M. Leda, K. E. Sawin, Remodeling of the fission yeast Cdc42 cell-polarity module via the Sty1 p38 stress-activated protein kinase pathway. *Curr. Biol.* **26**, 2921–2928 (2016).

25. L. Duan, J. Hope, Q. Ong, H. Y. Lou, N. Kim, C. McCarthy, V. Acero, M. Z. Lin, B. Cui, Understanding CRY2 interactions for optical control of intracellular signaling. *Nat. Commun.* **8**, 547 (2017).

26. J. Valdez-Taubas, H. R. Pelham, Slow diffusion of proteins in the yeast plasma membrane allows polarity to be maintained by endocytic cycling. *Curr. Biol.* **13**, 1636–1640 (2003).

27. H. Tatebe, K. Nakano, R. Maximo, K. Shiozaki, Pom1 DYRK regulates localization of the Rga4 GAP to ensure bipolar activation of Cdc42 in fission yeast. *Curr. Biol.* **18**, 322–330 (2008).

28. H. Brzeska, J. Guag, K. Remmert, S. Chacko, E. D. Korn, An experimentally based computer search identifies unstructured membrane-binding sites in proteins: Application to class I myosins, PAKS, and CARMIL. *J. Biol. Chem.* **285**, 5738–5747 (2010).

29. D. Gallo Castro, S. G. Martin, Differential GAP requirement for Cdc42-GTP polarization during proliferation and sexual reproduction. *J. Cell Biol.* **217**, 4215–4229 (2018).

30. A. Kusumi, T. K. Fujiwara, R. Chadda, M. Xie, T. A. Tsunoyama, Z. Kalay, R. S. Kasai, K. G. Suzuki, Dynamic organizing principles of the plasma membrane that regulate signal transduction: Commemorating the fortieth anniversary of Singer and Nicolson's fluid-mosaic model. *Annu. Rev. Cell Dev. Biol.* **28**, 215–250 (2012).

31. Z. Shi, Z. T. Graber, T. Baumgart, H. A. Stone, A. E. Cohen, Cell membranes resist flow. *Cell* **175**, 1769–1779.e13 (2018).

32. O. Hachet, M. Berthelot-Grosjean, K. Kokkoris, V. Vincenzetti, J. Moosbrugger, S. G. Martin, A phosphorylation cycle shapes gradients of the DYRK family kinase Pom1 at the plasma membrane. *Cell* **145**, 1116–1128 (2011).

33. N. N. Padte, S. G. Martin, M. Howard, F. Chang, The cell-end factor pom1p inhibits mid1p in specification of the cell division plane in fission yeast. *Curr. Biol.* **16**, 2480–2487 (2006).

34. S. G. Martin, M. Berthelot-Grosjean, Polar gradients of the DYRK-family kinase Pom1 couple cell length with the cell cycle. *Nature* **459**, 852–856 (2009).

35. J. B. Moseley, A. Mayeux, A. Paoletti, P. Nurse, A spatial gradient coordinates cell size and mitotic entry in fission yeast. *Nature* **459**, 857–860 (2009).

36. L. Deng, J. B. Moseley, Compartmentalized nodes control mitotic entry signaling in fission yeast. *Mol. Biol. Cell* **24**, 1872–1881 (2013).

37. M. Guzman-Vendrell, S. Baldissard, M. Almonacid, A. Mayeux, A. Paoletti, J. B. Moseley, Blt1 and Mid1 provide overlapping membrane anchors to position the division plane in fission yeast. *Mol. Cell. Biol.* **33**, 418–428 (2013).

38. S. Okada, M. Leda, J. Hanna, N. S. Savage, E. Bi, A. B. Goryachev, Daughter cell identity emerges from the interplay of Cdc42, septins, and exocytosis. *Dev. Cell* **26**, 148–161 (2013).

39. R. T. A. Pedersen, J. E. Hassinger, P. Marchando, D. G. Drubin, Spatial regulation of clathrin-mediated endocytosis through position-dependent site maturation. *J. Cell Biol.* **219**, e202002160 (2020).

40. M. Jose, S. Tollis, D. Nair, J. B. Sibarita, D. McCusker, Robust polarity establishment occurs via an endocytosis-based cortical corralling mechanism. *J. Cell Biol.* **200**, 407–418 (2013).

41. V. Gerganova, C. Floderer, A. Archetti, L. Michon, L. Carlini, T. Reichler, S. Manley, S. G. Martin, Multi-phosphorylation reaction and clustering tune Pom1 gradient mid-cell levels according to cell size. *eLife* **8**, e45983 (2019).

42. A. T. Layton, N. S. Savage, A. S. Howell, S. Y. Carroll, D. G. Drubin, D. J. Lew, Modeling vesicle traffic reveals unexpected consequences for Cdc42p-mediated polarity establishment. *Curr. Biol.* **21**, 184–194 (2011).

43. J. Lemière, Y. Ren, J. Berro, Rapid adaptation of endocytosis, exocytosis and eisosomes after an acute increase in membrane tension in yeast cells. *bioRxiv*, 342030 (2021).

44. G. Steinberg, M. A. Penalva, M. Riquelme, H. A. Wosten, S. D. Harris, Cell biology of hyphal growth. *Microbiol. Spectr.* **5**, (2017).

45. G. M. Griffiths, A. Tsun, J. C. Stinchcombe, The immunological synapse: A focal point for endocytosis and exocytosis. *J. Cell Biol.* **189**, 399–406 (2010).

46. J. Roos, R. B. Kelly, The endocytic machinery in nerve terminals surrounds sites of exocytosis. *Curr. Biol.* **9**, 1411–1414 (1999).

47. J. A. Castillo-Badillo, A. C. Bandi, S. Harlalka, N. Gautam, SRRF-stream imaging of optogenetically controlled furrow formation shows localized and coordinated endocytosis and exocytosis mediating membrane remodeling. *ACS Synth. Biol.* **9**, 902–919 (2020).

48. K. S. Gerien, J. Q. Wu, Molecular mechanisms of contractile-ring constriction and membrane trafficking in cytokinesis. *Biophys. Rev.* **10**, 1649–1666 (2018).

49. V. Y. Kiselev, D. Marenduzzo, A. B. Goryachev, Lateral dynamics of proteins with polybasic domain on anionic membranes: A dynamic Monte-Carlo study. *Biophys. J.* **100**, 1261–1270 (2011).

50. K. C. Vinnakota, D. A. Mitchell, R. J. Deschenes, T. Wakatsuki, D. A. Beard, Analysis of the diffusion of Ras2 in Saccharomyces cerevisiae using fluorescence recovery after photobleaching. *Phys. Biol.* **7**, 026011 (2010).

51. B. Khalili, L. Merlini, V. Vincenzetti, S. G. Martin, D. Vavylonis, Exploration and stabilization of Ras1 mating zone: A mechanism with positive and negative feedbacks. *PLOS Comput. Biol.* **14**, e1006317 (2018).

52. G. R. Hammond, Y. Sim, L. Lagnado, R. F. Irvine, Reversible binding and rapid diffusion of proteins in complex with inositol lipids serves to coordinate free movement with spatial information. *J. Cell Biol.* **184**, 297–308 (2009).

53. R. Iino, I. Koyama, A. Kusumi, Single molecule imaging of green fluorescent proteins in living cells: E-cadherin forms oligomers on the free cell surface. *Biophys. J.* **80**, 2667–2677 (2001).

54. D. T. Gillespie, Exact stochastic simulation of coupled chemical reactions. *J. Phys. Chem.* **81**, 2340–2361 (1977).

55. P. Castro-Villarreal, A. Villada-Balbuena, J. M. Mendez-Alcaraz, R. Castaneda-Priego, S. Estrada-Jimenez, A Brownian dynamics algorithm for colloids in curved manifolds. *J. Chem. Phys.* **140**, 214115 (2014).

56. A. W. McClure, M. Minakova, J. M. Dyer, T. R. Zyla, T. C. Elston, D. J. Lew, Role of polarized g protein signaling in tracking pheromone gradients. *Dev. Cell* **35**, 471–482 (2015).

57. H. Cheng, R. Sugiura, W. Wu, M. Fujita, Y. Lu, S. O. Sio, R. Kawai, K. Takegawa, H. Shuntoh, T. Kuno, Role of the Rab GTP-binding protein Ypt3 in the fission yeast exocytic pathway and its connection to calcineurin function. *Mol. Biol. Cell* **13**, 2963–2976 (2002).

58. N. Wang, I. J. Lee, G. Rask, J. Q. Wu, Roles of the TRAPP-II complex and the exocyst in membrane deposition during fission yeast cytokinesis. *PLOS Biol.* **14**, e1002437 (2016).

59. J. H. Lee, J. E. Heuser, R. Roth, U. Goodenough, Eisosome ultrastructure and evolution in fungi, microalgae, and lichens. *Eukaryot. Cell* **14**, 1017–1042 (2015).

60. W. Kukulski, M. Schorb, M. Kaksonen, J. A. Briggs, Plasma membrane reshaping during endocytosis is revealed by time-resolved electron tomography. *Cell* **150**, 508–520 (2012).

61. L. V. Chernomordik, M. M. Kozlov, Mechanics of membrane fusion. *Nat. Struct. Mol. Biol.* **15**, 675–683 (2008).

62. W. Shin, G. Arpino, S. Thiyagarajan, R. Su, L. Ge, Z. McDargh, X. Guo, L. Wei, O. Shupliakov, A. Jin, B. O'Shaughnessy, L. G. Wu, Vesicle shrinking and enlargement play opposing roles in the release of exocytotic contents. *Cell Rep.* **30**, 421–431.e7 (2020).

63. M. Chabanon, J. C. S. Ho, B. Liedberg, A. N. Parikh, P. Rangamani, Pulsatile lipid vesicles under osmotic stress. *Biophys. J.* **112**, 1682–1691 (2017).

64. B. Fogelson, A. Mogilner, Computational estimates of membrane flow and tension gradient in motile cells. *PLOS ONE* **9**, e84524 (2014).

65. A. E. Cohen, Z. Shi, Do cell membranes flow like honey or jiggle like jello? *BioEssays* **42**, 1900142t (2020).

66. K. D. Moran, D. J. Lew, How diffusion impacts cortical protein distribution in yeasts. *Cell* **9**, 1113 (2020).

67. Z. Kalay, T. K. Fujiwara, A. Otaka, A. Kusumi, Lateral diffusion in a discrete fluid membrane with immobile particles. *Phys. Rev. E* **89**, 022724 (2014).

68. S. S. Andrews, D. Bray, Stochastic simulation of chemical reactions with spatial resolution and single molecule detail. *Phys. Biol.* **1**, 137–151 (2004).

69. O. N. Yogurtcu, M. E. Johnson, Theory of bi-molecular association dynamics in 2D for accurate model and experimental parameterization of binding rates. *J. Chem. Phys.* **143**, 084117 (2015).

70. B. O'Shaughnessy, D. Vavylonis, Kinetic regimes and cross-over times in many-particle reacting systems. *Europhys. Lett.* **45**, 653–658 (1999).

71. J. Ries, C. Klose, C. Walch-Solimena, P. Schwille, How to measure slow diffusion in yeast cell membranes. *Proc. SPIE* **6991**, 69910w (2008).

72. J. Bahler, J. Q. Wu, M. S. Longtine, N. G. Shah, A. McKenzie, 3rd, A. B. Steever, A. Wach, P. Philippsen, J. R. Pringle, Heterologous modules for efficient and versatile PCR-based gene targeting in Schizosaccharomyces pombe. *Yeast* **14**, 943–951 (1998).

73. A. Vjestica, M. Marek, P. J. Nkosi, L. Merlini, G. Liu, M. Berard, I. Billault-Chaumartin, S. G. Martin, A toolbox of Stable Integration Vectors (SIV) in the fission yeast Schizosaccharomyces pombe. *J. Cell Sci.* **113**, jcs240754 (2019).

74. F. O. Bendezu, S. G. Martin, Actin cables and the exocyst form two independent morphogenesis pathways in the fission yeast. *Mol. Biol. Cell* **22**, 44–53 (2011).

75. O. Dudin, F. O. Bendezu, R. Groux, T. Laroche, A. Seitz, S. G. Martin, A formin-nucleated actin aster concentrates cell wall hydrolases for cell fusion in fission yeast. *J. Cell Biol.* **208**, 897–911 (2015).

76. H. Wang, X. Tang, J. Liu, S. Trautmann, D. Balasundaram, D. McCollum, M. K. Balasubramanian, The multiprotein exocyst complex is essential for cell separation in Schizosaccharomyces pombe. *Mol. Biol. Cell* **13**, 515–529 (2002).

77. B. P. Ziemba, J. D. Knight, J. J. Falke, Assembly of membrane-bound protein complexes: Detection and analysis by single molecule diffusion. *Biochemistry* **51**, 1638–1647 (2012).

78. J. D. Knight, M. G. Lerner, J. G. Marcano-Velazquez, R. W. Pastor, J. J. Falke, Single molecule diffusion of membrane-bound proteins: Window into lipid contacts and bilayer dynamics. *Biophys. J.* **99**, 2879–2887 (2010).

79. B. A. Camley, F. L. H. Brown, Motion of objects embedded in lipid bilayer membranes: Advection and effective viscosity. *J. Chem. Phys.* **151**, 124104 (2019).

80. J. R. Houser, D. J. Busch, D. R. Bell, B. Li, P. Y. Ren, J. C. Stachowiak, The impact of physiological crowding on the diffusivity of membrane bound proteins. *Soft Matter* **12**, 2127–2134 (2016).

81. D. F. Kucik, E. L. Elson, M. P. Sheetz, Weak dependence of mobility of membrane protein aggregates on aggregate size supports a viscous model of retardation of diffusion (vol 76, pg 314, 1999). *Biophys. J.* **76**, 1720–1720 (1999).

82. J. Chow, Correlation Matrix Scatterplot, in *MATLAB Central File Exchange* (2020); www.mathworks.com/matlabcentral/fileexchange/53043-correlation-matrix-scatterplot [accessed 12 August 2020].

83. F. O. Bendezu, V. Vincenzetti, S. G. Martin, Fission yeast Sec3 and Exo70 are transported on actin cables and localize the exocyst complex to cell poles. *PLOS ONE* **7**, e40248 (2012).

84. J. Q. Wu, J. Bahler, J. R. Pringle, Roles of a fimbrin and an alpha-actinin-like protein in fission yeast cell polarization and cytokinesis. *Mol. Biol. Cell* **12**, 1061–1077 (2001).

85. V. Sirotkin, J. Berro, K. Macmillan, L. Zhao, T. D. Pollard, Quantitative analysis of the mechanism of endocytic actin patch assembly and disassembly in fission yeast. *Mol. Biol. Cell* **21**, 2894–2904 (2010).

86. M. Kohli, V. Galati, K. Boudier, R. W. Roberson, P. Philippsen, Growth-speed-correlated localization of exocyst and polarisome components in growth zones of Ashbya gossypii hyphal tips. *J. Cell Sci.* **121**, 3878–3889 (2008).

87. N. Taheri-Talesh, T. Horio, L. Araujo-Bazan, X. Dou, E. A. Espeso, M. A. Penalva, S. A. Osmani, B. R. Oakley, The tip growth apparatus of Aspergillus nidulans. *Mol. Biol. Cell* **19**, 1439–1449 (2008).

88. D. L. Delgado-Alvarez, O. A. Callejas-Negrete, N. Gomez, M. Freitag, R. W. Roberson, L. G. Smith, R. R. Mourino-Perez, Visualization of F-actin localization and dynamics with live cell markers in Neurospora crassa. *Fungal Genet. Biol.* **47**, 573–586 (2010).

89. D. McCusker, A. Royou, C. Velours, D. Kellogg, Cdk1-dependent control of membrane-trafficking dynamics. *Mol. Biol. Cell* **23**, 3336–3347 (2012).

90. J. Y. Tinevez, N. Perry, J. Schindelin, G. M. Hoopes, G. D. Reynolds, E. Laplantine, S. Y. Bednarek, S. L. Shorte, K. W. Eliceiri, TrackMate: An open and extensible platform for single-particle tracking. *Methods* **115**, 80–90 (2017).

91. J. Huang, Y. Huang, H. Yu, D. Subramanian, A. Padmanabhan, R. Thadani, Y. Tao, X. Tang, R. Wedlich-Soldner, M. K. Balasubramanian, Nonmedially assembled F-actin cables incorporate into the actomyosin ring in fission yeast. *J. Cell Biol.* **199**, 831–847 (2012).